JGR Solid Earth

RESEARCH ARTICLE
10.1029/2024JB030888

GNSS and InSAR Integration for 3-D Crustal Deformation in California and Western Nevada

Z.-K. Shen[1] **and Z. Liu**[2]

[1]Department of Earth, Planetary, and Space Science, UCLA, Los Angeles, CA, USA, [2]Jet Propulsion Laboratory, California Institute of Technology, Pasadena, CA, USA

Key Points:

- Global navigation satellite system and interferometric synthetic aperture radar data are integrated for mapping precise 3-D crustal deformation in California and western Nevada using an original method
- Deformation field is broadly distributed across the San Andreas and Walker Lane fault systems, suggesting ductile flow in the lower crust
- Hydrologic-related vertical deformation is widely observed, including large subsidence in Central Valley and vertical offsets across faults

Supporting Information:

Supporting Information may be found in the online version of this article.

Correspondence to:

Z.-K. Shen and Z. Liu,
zshen@ucla.edu;
zhen.liu@jpl.nasa.gov

Citation:

Shen, Z.-K., & Liu, Z. (2025). GNSS and InSAR integration for 3-D crustal deformation in California and western Nevada. *Journal of Geophysical Research: Solid Earth*, *130*, e2024JB030888. https://doi.org/10.1029/2024JB030888

Received 1 DEC 2024
Accepted 29 SEP 2025

Author Contributions:

Conceptualization: Z.-K. Shen, Z. Liu
Data curation: Z.-K. Shen, Z. Liu
Formal analysis: Z.-K. Shen, Z. Liu
Funding acquisition: Z.-K. Shen, Z. Liu
Investigation: Z.-K. Shen, Z. Liu
Methodology: Z.-K. Shen, Z. Liu
Project administration: Z.-K. Shen
Resources: Z.-K. Shen, Z. Liu
Software: Z.-K. Shen
Supervision: Z.-K. Shen
Validation: Z.-K. Shen
Visualization: Z.-K. Shen
Writing – original draft: Z.-K. Shen, Z. Liu

Abstract The regions of California and Nevada are shaped by dynamic tectonic and hydrologic processes that drive significant crustal deformation. In this study we use the method of Shen and Liu (2020), https://doi.org/10.1029/2019ea001036 to integrate Global Navigation Satellite System (GNSS) and Interferometric Synthetic Aperture Radar (InSAR) observations to investigate deformation from both tectonic and hydrologic activities. This method includes interpolating GNSS velocity data into a continuous velocity field, evaluating uncertainties in GNSS and InSAR measurements, correcting orbital errors in InSAR data, and combining InSAR Line-of-Sight measurements with GNSS data to resolve 3-D deformation using least squares regression. We apply this method to three decades of GNSS and InSAR data across California and western Nevada. Key findings include: (a) Faulting along the San Andreas and Walker Lane fault systems drives dextral shear motions of 30–40 and 8–12 mm/yr, respectively. Residual deformation, however, is broadly distributed within the fault systems, particularly in the Walker Lane region, suggesting contributions from ductile flow in the lower crust. (b) Significant subsidence, caused by drought and excessive groundwater withdrawal, is observed in the San Joaquin and Sacramento Valleys, at rates of 150–250 and 10–25 mm/yr, respectively. Uplift rebound of 3–8 mm/yr is observed in the mountains surrounding the San Joaquin Valley. Notable subsidence of 6–14 mm/yr is also seen along the California coastline, while the Santa Maria Basin and Oxnard Plain experience subsidence of up to 12–18 mm/yr. (c) Abrupt vertical offsets are observed across various tectonically active faults, suggesting fault-modulated hydrological deformation.

Plain Language Summary The regions of California and Nevada are shaped by dynamic tectonic and hydrologic processes that contribute to significant crustal deformation. Monitoring and understanding these deformation phenomena are essential for assessing seismic hazards, managing groundwater resources, and mitigating risks to infrastructure and communities. In this study we use the method of Shen and Liu (2020), https://doi.org/10.1029/2019ea001036 to integrate GNSS and InSAR observations to investigate crustal deformation associated with both tectonic and hydrologic activities. We apply the method to probe crustal deformation across California and western Nevada. Up to three decades of data are incorporated, and the results reveal: (a) In the plate boundary zone, tectonic deformation is dominated by faulting around the San Andreas and Walker Lane fault systems. Nevertheless, significant residual deformation remains and is broadly distributed, particularly across the Walker Lane fault system, suggesting contribution from ductile flow in the lower crust. (b) Significant subsidence is observed in the Central Valley, around tens of centimeters annually due to drought and groundwater extraction. Subsidence of millimeters per year is also seen along the California coastline. (c) Abrupt vertical offsets are observed across various tectonically active faults, suggesting hydrological deformation modulated by faults acting as hydraulic barriers.

1. Introduction

California and Nevada are situated within a broad boundary zone between the Pacific and North America plates. Tectonic activities, such as fault slip and folding along the San Andreas and the Walker Lane fault systems, lead to elastic and permanent crustal deformation (Bird, 2009; Hamilton & Myers, 1966) (Figure 1). Some of the regions in the boundary zone also experience significant fluid-related activities, including oil and gas production, groundwater extraction for agricultural and urban use, and reservoir impoundment for water storage and flood control. The interaction between tectonic and fluid processes influences surface deformation, leading to subsidence, uplift, and lateral displacements.

Writing – review & editing: Z.-K. Shen, Z. Liu

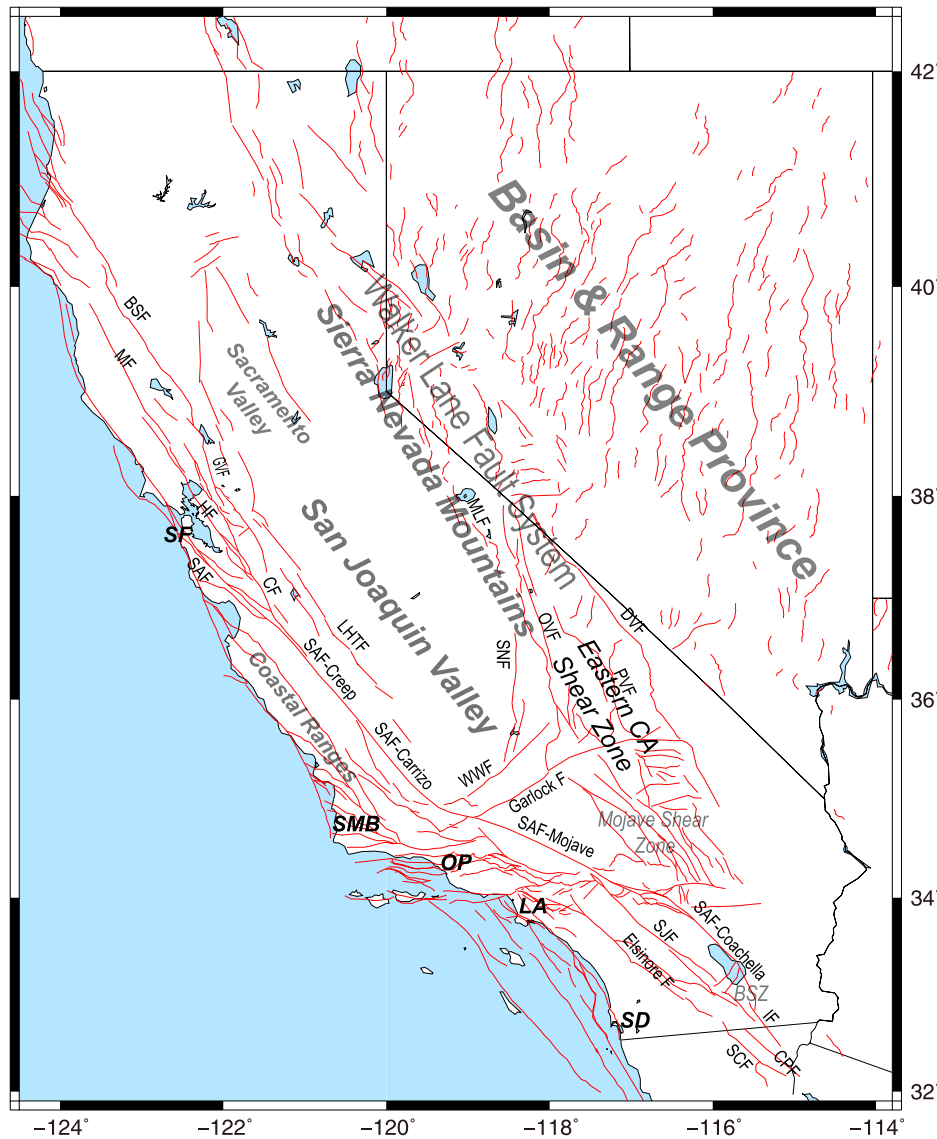

Figure 1. Tectonic setting of California and western Nevada. Red lines are geological faults from Hatem, Reitman, et al. (2022). Abbreviations of fault and location names: BSF, Bartlett Springs fault; BSZ, Brawley Seismic Zone; Carrizo, Carrizo Plain segment; CF, Calaveras fault; CPF, Cerro Prieto fault; Creep, Central California Creep segment; Coachella, Coachella Valley segment; DVF, Death Valley fault; GVF, Green Valley fault; HF, Hayward fault; IF, Imperial fault; LHTF, Lost Hill Thrust fault; MF, Maacama fault; MLF, Mono Lake fault; OVF, Owens Valley fault; PVF, Panamint Valley fault; SAF, San Andreas fault; SCF, Sierra Cucapah fault; SJF, San Jacinto fault; SNF, Sierra Nevada fault; LA, Los Angeles; OP, Oxnard Plain; SD, San Diego; SF, San Francisco; SMB, Santa Maria Basin.

Precise measurements of crustal deformation in California were initially carried out in the 1960s and 1970s using the electronic distance ranging technique, with the surveys primarily carried out along the San Andreas fault system (SAFS) to measure slip rates along sections of the faults (Lisowski et al., 1991). Since the late 1980s, global navigation satellite system (GNSS) (specifically Global Positioning System (GPS)) networks have been established across California and Nevada, and the measurements were carried out initially in survey-mode and increasingly in continuous mode, to quantify strain accumulation along faults, measure earthquake-related deformation, and assess seismic hazards and hydraulic impacts (e.g., Borsa et al., 2014; d'Alessio et al., 2005; Dixon et al., 2000; Feigl et al., 1993; Hammond et al., 2011; Johnson, 2024; Klein et al., 2019; Kreemer & Young, 2022; Pollitz et al., 2022; Petersen et al., 2024; Shen et al., 2011).

Interferometric Synthetic Aperture Radar (InSAR) techniques provide a complementary method for monitoring surface deformation across large areas with high spatial resolution. The radar phase difference between acquisitions, called an interferogram, records the change in distance between radar instrument and the Earth's surface over time. By analyzing the radar interferograms derived from satellite data, InSAR enables the detection of subtle surface changes associated with tectonic and hydrologic processes. In California and Nevada, InSAR studies have revealed patterns of tectonic deformation along the SAFS (e.g., Fialko, 2006; Xu et al., 2021), as well as land subsidence due to groundwater extraction in agricultural regions such as the San Joaquin Valley (SJV) (e.g., Liu et al., 2019; Neely et al., 2021).

Most crustal deformation studies to date in California and other parts of the world have been using either GPS or InSAR, although a number of studies have also pioneered to integrate GPS and InSAR data for a more comprehensive analysis (e.g., Bürgmann et al., 2006; Fang et al., 2024; Tong et al., 2013; Weiss et al., 2020; Xu et al., 2021; Ward et al., 2021; Yan et al., 2022). GPS and InSAR data complement each other in resolving crustal deformation. Survey-mode GPS provides 2-D horizontal and continuous GPS offers 3–D displacements at discretized sites while InSAR presents detailed maps of surface displacement, but only in the line-of-sight (LOS) direction. Using data acquired from both ascending and descending satellite orbits enables measurements of two different directions, but is still not capable of resolving 3–D displacements without additional data integration or assumptions. Integrated analyses of GNSS and InSAR data facilitate the assessment of 3-D deformation field with high-resolution spatial coverage for the detection of localized deformation features, quantification of strain accumulation along fault systems, and characterization of hydrologic activities. The approach can help address some long-standing scientific questions, such as how are tectonic strains distributed in California and Nevada and what are the driving mechanisms? How much is the off-fault strain and how is it distributed? Where is the accumulated seismic moment distributed along the plate boundary zone? How fast is groundwater depletion in the Central Valley and where is it distributed? How are the hydraulic activities interacting with the fault systems? The integrated deformation model presented here aims to address these questions, and as discussed in the results, reveals new and sometimes unexpected findings with potentially wide-reaching implications.

2. GNSS and InSAR Data

2.1. GNSS Data

We acquire GNSS velocity data from two primary sources. The first data set is from the velocity solution of continuous GNSS sites in western United States, produced by the NASA-Scripps MEaSUREs project (http://sopac-csrc.ucsd.edu/index.php/velocities/). These station velocities were derived from measurements of the last 2–3 decades under the ITRF2014 reference frame, and subsequently transformed to the North America reference frame (Altamimi et al., 2017) (Figures 2 and 3). For each GNSS site the position time series is modeled to determine initial position, secular velocity, position jumps due to earthquakes or instrumental changes, and postseismic displacements modeled as exponential or logarithmic functions if affected by major earthquakes (Bock et al., 2021), and the station secular velocities obtained from the analysis are adopted for this study.

The second data set is from Zeng (2022a), which synthesized campaign and continuous GNSS velocity solutions from seven sources. These data primarily include processing by the UCLA group of campaign GNSS data in western US (Shen, 2017) and by the Nevada Geodetic Lab (NGL) of data from the western Nevada network (http://geodesy.unr.edu/). The velocity solution from the UCLA group was produced following a similar procedure of Shen et al. (2011). The velocity solution from the NGL was obtained following a different processing procedure of Blewitt et al. (2016). To ensure consistency, these velocities were rotated to align with the MEaSUREs' solution by minimizing the postfit residuals of common sites across solutions. Sites from Zeng's compilation that overlap or are within 1 km of the MEaSUREs sites are excluded. Unlike the MEaSUREs data set, the GNSS velocities from Zeng (2022a) include only the horizontal components. We inspected the combined velocity field and filtered out outliers and sites with horizontal velocity uncertainties greater than 2 mm/yr. We use GNSS sites located within the region of (32.0°N–42.5°N, 125.0°W–113.5°W) for this study (Figure 2), with the data set tabulated in Data S1 in Supporting Information S1 (Shen & Liu, 2025) and site velocities illustrated in Figure 3.

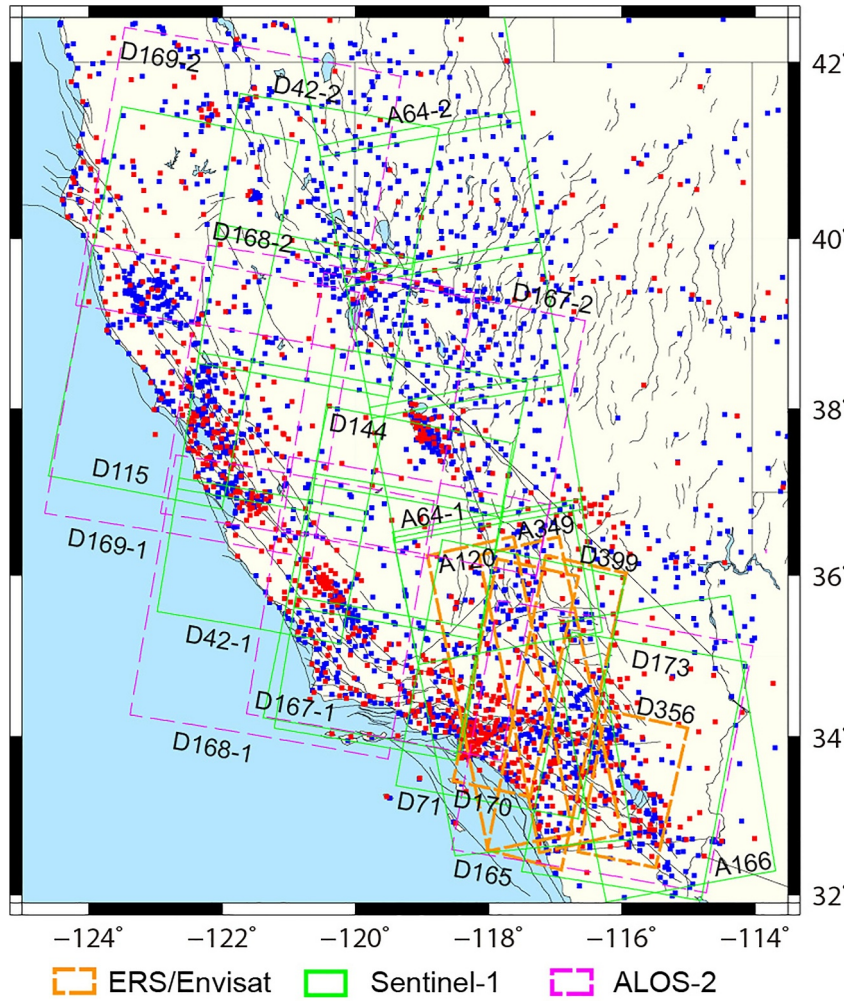

Figure 2. Study area in California and western Nevada. Black curves are active faults, red and blue squares are global navigation satellite system sites whose 3D and 2D (horizontal only) data are used in this study respectively. The orange, green, and magenta frames denote the ground footprints of ERS/Envisat, Sentinel-1, and ALOS-2 interferometric synthetic aperture radar tracks whose data are used in this study.

2.2. InSAR Data

Synthetic Apture Radar (SAR) data from multiple satellite sensors are acquired and processed for this study, whose ground footprints of tracks cover the region of California and western Nevada (Figure 2). The data include C-band ERS/Envisat, Sentinel-1 (S-1), and L-band ALOS-2 ScanSAR acquisitions. The ERS/Envisat data span the period of 1992–2010, and the S-1 and ALOS-2 ScanSAR sensors have been collecting data in California and western Nevada since late 2014. The time spans for individual tracks of the satellites are listed in Table S1 in Supporting Information S1.

The ERS-1,2 and Envisat data are processed using a modified version of JPL/Caltech ROI_PAC software package. The InSAR Scientific Computing Environment (ISCE) software is used to process the S-1 and ALOS-2 data and generate interferograms (Rosen et al., 2012). General processing steps include interferometric phase flattening using precise orbit, topography phase correction, phase unwrapping, filtering and geocoding. For the ERS-2 data after 2001 that have Doppler issue due to gyroscope failure, we employ a maximum entropy approach to resolve Doppler ambiguity and identify all usable ERS-2 interferometric pairs. For Envisat ASAR sensors, we correct temporally correlated range ramp error due to long-term local oscillator frequency drift by adopting an empirical approach (Marinkovic & Larsen, 2013). For ERS and Envisat, orbital ramp error from the same track is

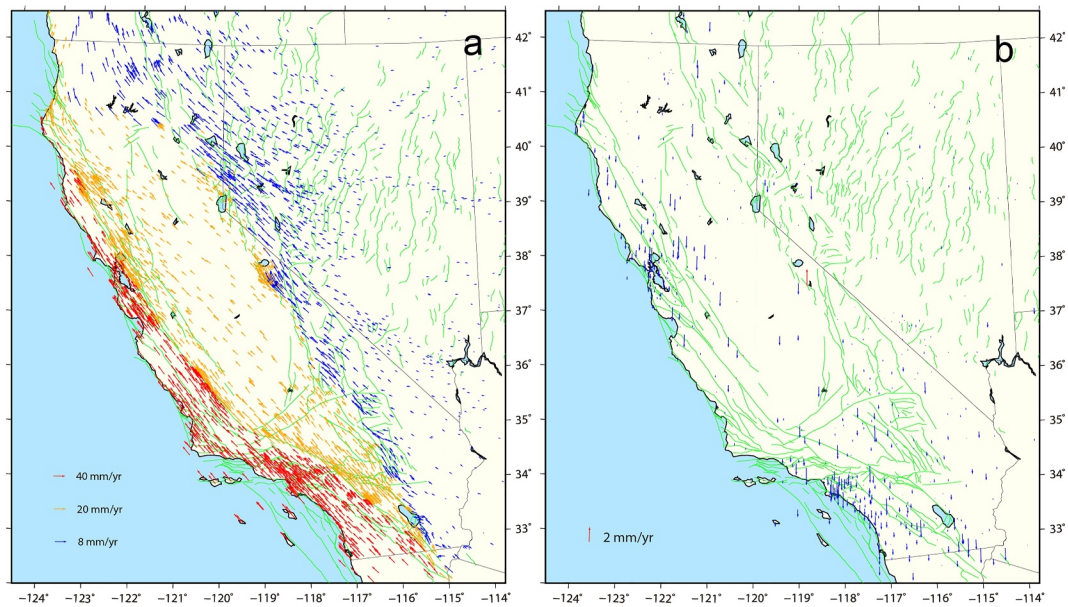

Figure 3. Global navigation satellite system velocity data used, referenced to North American plate. (a) and (b) are for the horizontal and vertical components, respectively. Three colors used in (a) denote the horizontal velocities at different amplitude scales. Red and blue arrows in (b) represent the upward and downward velocities.

typically limited to a few acquisitions and small (Fattahi & Amelung, 2014), we correct only affected interferograms through baseline re–estimation with the constraint of a priori GNSS based deformation model. For S-1 data, we use a stack processor to co-register all SAR images to the same reference geometry and employ an enhanced spectral diversity technique to estimate azimuth misregistration between all SLC images in a stack sense (Fattahi et al., 2017). For L-band ALOS-2 data, we apply a range split-spectrum approach (Liang & Fielding, 2017a, 2017b; Liang et al., 2018) to estimate ionosphere phase artifacts and correct them from the interferograms. We use a variant of the Small Baseline Subset InSAR time series approach to solve for InSAR LOS time series and mean velocity (e.g., Liu et al., 2019; Sansosti et al., 2010). Thousands of interferograms that meet spatial and temporal baseline criteria are formed and used in the time series inversion. We incorporate topography dependent troposphere delay correction, residual DEM error and employ spatiotemporal filtering to remove high frequency turbulent troposphere noise (Liu et al., 2014, 2019; Samsonov, 2010). The SAR tracks/frames and time spans not influenced by earthquake induced deformation signals are used in the analysis (see Table S1 in Supporting Information S1). In the postprocessing stage we adopt a Jackknife variance estimation approach (Efron & Stein, 1981) to characterize the uncertainties associated with the InSAR deformation map. The approach provides a reasonable way to account for uncertainties arisen from lacking or missing dates, uncorrected residuals or other noises, and/or the influence of reference pixel and date. All the InSAR LOS data used in this study are shown in Figure S1 in Supporting Information S1.

3. GNSS and InSAR Data Integration

We extend an algorithm developed by (Shen & Liu, 2020) to integrate the GNSS and InSAR data and derive a 3-D velocity field for California and western Nevada. This process consists of four main steps and is described below.

In step one, we interpolate the discrete GNSS velocities into a continuous field with a grid size of 0.02°-N × 0.02°E, following an optimized approach developed by Shen et al. (2015). We also estimate realistic uncertainties for the interpolated GNSS velocities, to be used as weights for GNSS data in GNSS and InSAR combination. The estimation involves: (a) using differential velocities of closely spaced station pairs to set minimum uncertainty thresholds, which are determined to be 0.4 mm/yr for horizontal and 0.6 mm/yr for vertical components. (b) Interpolating the GNSS velocities and their uncertainties to create a continuous velocity field, with a varying degree of smoothing at each site determined by balancing a trade-off between the spatial resolution and solution stability (Shen & Liu, 2020; Shen et al., 2015) (Figure S2 in Supporting Information S1). (c) Using

bootstrapping algorithm to calibrate interpolated GNSS velocity uncertainties by adjusting the smoothing distance in the assessment. The estimation is performed in an iteration, each time an apriori smoothing distance factor is assumed, and used uniformly to evaluate the interpolation velocity and its uncertainty (σ_a) at each GNSS site without using data of the site, and a difference (σ_d) is calculated at the site between the estimated and original site velocities. Two median uncertainty estimates of all the sites (σ_{am} and σ_{dm}) are compared, and another iteration is run with a new apriori smoothing distance, until the two median uncertainties align closely. Range distribution histograms of σ_a and σ_d for the three velocity components show that they are largely comparable (Figure S3 in Supporting Information S1).

In step two, we use the same grid size of 0.02°N × 0.02°E, and take the average of InSAR data per grid cell for each track, including the LOS velocity, azimuth angle, look direction, and LOS uncertainty. The binned LOS data are then compared with GNSS data to determine the scale factors for LOS velocity uncertainties. Specifically, for each selected track, we take the GNSS data as ground truth, compute differences between the (de-meaned) LOS data and GNSS-projected LOS values at grid cells where GNSS data are available, and use the RMS of differences to scale the InSAR data uncertainties (Figure S4 in Supporting Information S1). The scaling factors are listed in Table S2 in Supporting Information S1.

In step three, we estimate offsets and ramps for the InSAR LOS velocities of different tracks, resulting from residual orbital error and/or atmospheric/ionospheric noise. Since InSAR data provide only LOS measurements, these offset/ramp parameters need to be estimated together with the 3-D ground velocities. We use two subsets of GNSS data at grid points to stabilize this estimate: the first includes all grid points with direct GNSS velocity observations, while the second consists of decimated grid points with multiple InSAR data entries and interpolated GNSS velocities. This second subset reinforces offset/ramp solutions, especially for tracks with sparse or uneven GNSS coverage. Decimation by a factor of 20 per dimension (0.4° for 0.02° cell spacing) is sufficient. The formulation of the modeling procedure is the following: For the ith InSAR track of the jth LOS observations at the kth gird cell O_{ijk}, we have:

$$O_{ijk} = \underline{D_{ijk}} \cdot \underline{V_k} + \underline{P_{ijk}} \cdot \underline{R_i} + \varepsilon_{ijk} \tag{1}$$

where $\underline{V_k} = (V_{e\_k}, V_{n\_k}, V_{u\_k})^{\mathrm{T}}$ is the 3-D velocity components to be solved at the kth grid point on earth ($k = 1$ to l), $\underline{D_{ijk}} = (-\sin\theta_{ijk}\cos\alpha_{ijk}, \sin\theta_{ijk}\sin\alpha_{ijk}, \cos\theta_{ijk})$ is the unit vector to project $\underline{V_k}$ to the LOS direction ($i = 1$ to m and $j = 1$ to n), and θ_{ijk} and α_{ijk} are the incidence angle and athmuth angle of the jth radar beam from the ith satellite to the kth grid cell. $\underline{R_i} = (R_{0i}, R_{ei}, R_{ni})^{\mathrm{T}}$ represents the offset/ramp parameters for the ith satellite imagery, and $\underline{P_{ijk}} = (1, \Delta E_{ijk}, \Delta N_{ijk})$ links the offset/ramp correction terms to the LOS observation, and ΔE_{ijk} and ΔN_{ijk} are the east and north distance measured between the kth grid cell and the center of the ith satellite imagery. ε_{ijk} is the InSAR observation error. The equations in matrix form are:

$$\begin{bmatrix} O_{111} \\ U_1 \\ \vdots \\ O_{ijk} \\ U_k \\ \vdots \\ O_{mnl} \\ U_l \end{bmatrix} = \begin{bmatrix} D_{111} & 0 & \vdots & \vdots & 0 & P_1 & 0 & \vdots & \vdots & 0 \\ I & 0 & \vdots & \vdots & \vdots & \vdots & \vdots & \vdots & \vdots & 0 \\ \vdots & \vdots & \vdots & \vdots & \vdots & \vdots & \vdots & \vdots & \vdots & \vdots \\ 0 & \vdots & D_{ijk} & 0 & \vdots & \vdots & 0 & P_i & \vdots & 0 \\ \vdots & \vdots & I & 0 & \vdots & \vdots & \vdots & \vdots & \vdots & 0 \\ \vdots & \vdots & \vdots & \vdots & \vdots & \vdots & \vdots & \vdots & \vdots & \vdots \\ 0 & \vdots & \vdots & \vdots & D_{mnl} & 0 & \vdots & \vdots & \vdots & P_m \\ 0 & \vdots & \vdots & \vdots & I & 0 & \vdots & \vdots & \vdots & 0 \end{bmatrix} \begin{bmatrix} V_1 \\ \vdots \\ V_k \\ \vdots \\ V_l \\ R_1 \\ \vdots \\ R_i \\ \vdots \\ R_m \end{bmatrix} + \begin{bmatrix} \varepsilon_{111} \\ \varepsilon_1 \\ \vdots \\ \varepsilon_{ijk} \\ \varepsilon_k \\ \vdots \\ \varepsilon_{mnl} \\ \varepsilon_l \end{bmatrix} \tag{2}$$

where $\underline{U_k}=(U_{e\_k}, U_{n\_k}, U_{n\_k})^{\mathrm{T}}$ is the 3-D GNSS velocity observation data (directly measured or interpolated) at the kth grid cell, I is a 3 × 3 unit matrix, and $\underline{\varepsilon_i} = (\varepsilon_{e\_i}, \varepsilon_{n\_i}, \varepsilon_{u\_i})^{\mathrm{T}}$ is the error vector of the GNSS velocities. It should be noted that a grid cell may have more than one InSAR data points, and in that case multiple corresponding InSAR data are entered in the equations related to that grid cell.

We rewrite Equation 2 in the form of

$$\underline{y} = A\,\underline{x} + \underline{\varepsilon}, \qquad \underline{\varepsilon} \sim \mathrm{N}(0, C) \tag{3}$$

where C is the variance/covariance matrix of the observables obtained from InSAR data analysis and re-evaluation of the interpolated GNSS velocities. The final solution is obtained via least-squares regression:

$$\underline{x} = \left(A^{\mathrm{T}} C^{-1} A\right)^{-1} A^{\mathrm{T}} C^{-1} \underline{y} \tag{4}$$

In this solution vertical GNSS data in areas with rapid subsidence from groundwater or oil extraction are excluded.

In the last step, we remove contributions of offset and ramp components from the InSAR LOS data and solve for the 3-D velocity for each grid cell through least squares regression, incorporating interpolated GNSS velocities and all LOS data within each cell. Adaptive and rescaled GNSS and InSAR data uncertainties are used to weight the inputs. GNSS vertical data are excluded from the final solution, due to limited capacity in representing sites with rapid lateral variation in vertical deformation, particularly in areas affected by hydrological activities. For further details on the integration method please refer to Shen and Liu (2020). The software GIC3D and the solution file package are accessible at Shen and Liu (2025).

4. Results

4.1. Horizontal Deformation Field

Figure 4 illustrates the integrated horizontal amplitude and vertical velocity field for California and western Nevada, with respect to the North America plate, along with their uncertainties. The east and north velocity components and their uncertainties are shown in Figure S5 in Supporting Information S1, and Figure 5 displays 3-D velocity profiles trending perpendicular to the Pacific-North America relative plate motion direction, derived using the euler pole of relative plate motion (49.30°E, 76.01°S) from Kreemer et al. (2014).

We observe a remarkable agreement between the GNSS-measured and model-predicted horizontal velocities, with discrepancies of only 1–2 mm/yr or less across most of the region (Figures 5a and 5b). This agreement is primarily due to the robust constraint provided by the GNSS data on the horizontal velocity field, which has uncertainties of less than 2 mm/yr for interpolated components in most of the region (Figure S2b in Supporting Information S1). Additionally, InSAR data align well with the GNSS results, producing a unified velocity solution with 1–2 mm/yr precision that fills spatial gaps, including those in eastern California, the SJV, and near numerous active fault segments. Only a small portion of the study area, such as southwest Arizona, the northeastern corner of the research area, and two small patches in northern Sacramento Valley and southwestern SJV exhibits uncertainties reaching up to ∼5 mm/yr. Some regions with slightly larger horizontal velocity uncertainties, around 2–4 mm/yr, include other patches in the SJV, Sacramento Valley, near the northern California coast, and the southern Mojave Desert. Elsewhere in California and western Nevada, horizontal velocity uncertainties are generally 0.5–1.5 mm/yr, offering a detailed and precise deformation field across the region.

Our analysis reveals that horizontal deformation along the plate boundary in California and western Nevada is broadly distributed, with dextral shear motion observed across the entire region except for southeastern California (east of the Mojave Shear Zone and Coachella Valley SAF section), and in the SJV and Sacramento Valleys (Figures 4a and 5a). The SAFS displays the most significant deformation gradient, with rates of ∼40 mm/yr in southern California (from the Imperial fault [IF] to the Coachella SAF section), ∼35 mm/yr through central California (from the Mojave SAF section to the Hayward fault [HF]), and ∼30 mm/yr in northern California (from the Roger Creek to Maacama faults). Broad deformation is also noted across the Walker Lane fault system (WLFS) and the Eastern California Shear Zone (ECSZ), with dextral shear rates of ∼12 mm/yr across the Mojave

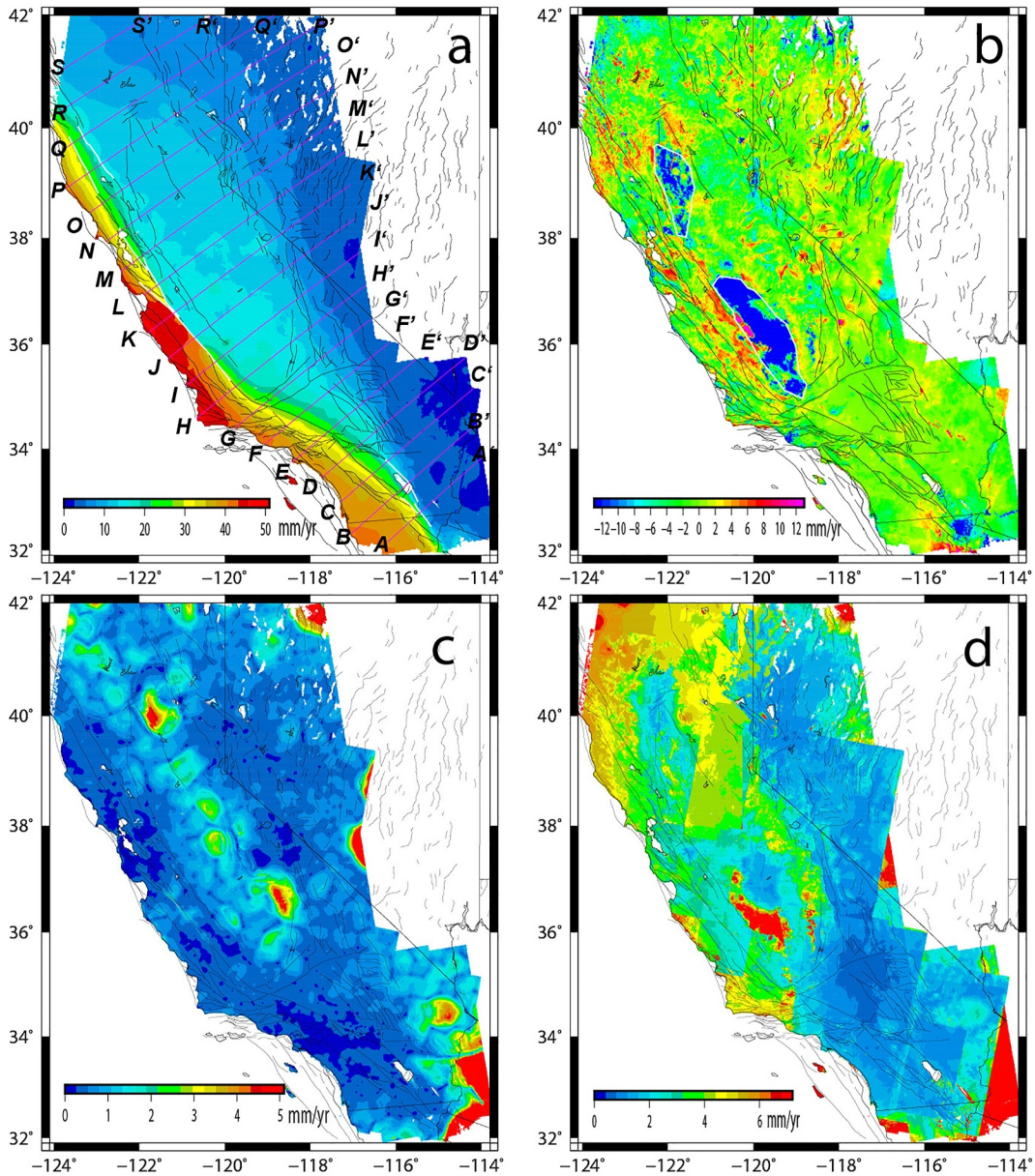

Figure 4. Integrated 3-D velocity field of California and western Nevada, with respect to stable North America. (a) and (b) are amplitudes of the horizontal and vertical velocities, and (c) and (d) are uncertainties of the horizontal and vertical components, respectively. White lines on faults mark creep segments across which discontinuous deformation is allowed in model representation. Magenta lines in (a) are locations of profiles along which components of velocity solutions are shown in Figure 5. White frames in (b) delineate the areas in San Joaquin Valley and Sacramento Valley in which significant subsidence takes place and the global navigation satellite system vertical data are not used for estimation of Synthetic Apture Radar orbital ramps and correction of their effects.

Shear Zone and 8–10 mm/yr across the central and northern Walker Lane (Figures 1, 4a, and 5a). The two fault systems converge southward into the Transverse Ranges deformation zone around the Big Bend of the SAF, and northward into the Cascadia deformation zone north of the Sacramento valley.

Normal deformation relative to the plate motion direction is generally small and undetectable in most areas (Figures 5c and 5d), with some notable exceptions: (a) Approximately 3 mm/yr of extension occurs across southern Mojave Shear Zone, due to deformation around the eastern syntax of the Big Bend of the SAF (profile *D–D′*, Figure 5c). (b) About 2–4 mm/yr of shortening across the western Transverse Ranges results from oblique

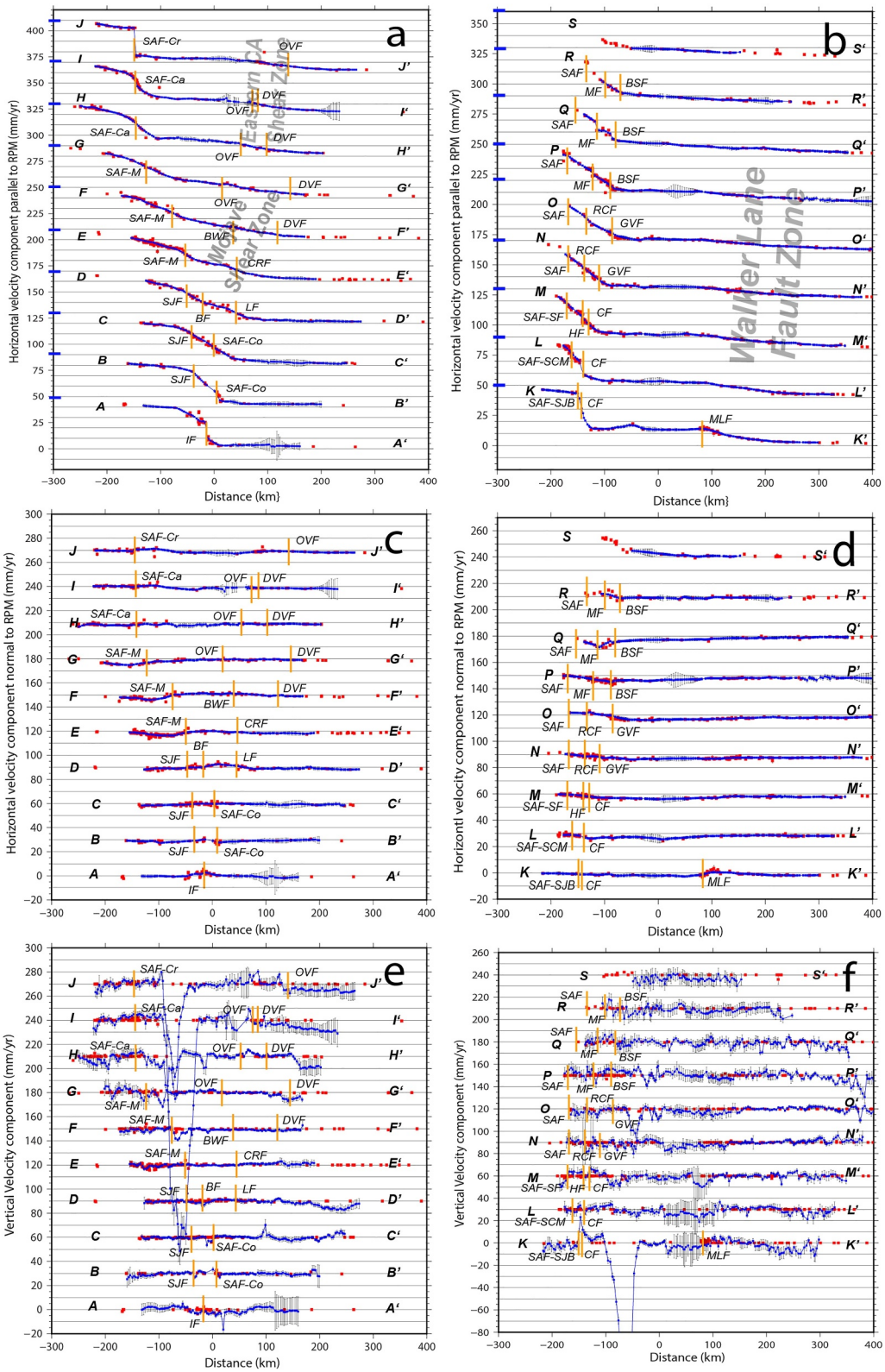

Figure 5.

convergence around the Big Bend of the SAF (profiles *E*–*E*′, *F*–*F*′, and *G*–*G*′, Figure 5c). (c) Shortening of ∼3–5 mm/yr is detected across the northern SAFS, possibly related to the clockwise bending of the SAF and underthrusting of the Juan de Fuca plate underneath the North America plate to the north (profiles *O*–*O*′ to *R*–*R*′, Figure 5d). (d) Convergence rates exceed 10 mm/yr north of the Mendocino triple junction in coastal northern California, again likely due to the Juan de Fuca plate's thrusting underneath the North American plate (profile *S*–*S*′, Figure 5d). No detectable internal deformation is found in the southern and eastern Mojave Desert, the SJV, and the Sacramento Valley.

Abrupt shear motion jumps are evident across various creeping faults, including the Coachella, Cholame, central California creep, San Juan Bautista (SJB), and Santa Cruz Mountains (SCM) sections of the SAF, as well as the Imperial, Superstition Hills, Calaveras, Bartlett Springs, and Maacama faults (Figures 5a and 5b). When modeling deformation near creeping faults, we exclude GNSS data points located on the opposite side of the fault relative to the evaluation point during the interpolation, in order to avoid smoothing out the sharp gradient signals across the fault (Figure S7 in Supporting Information S1) (Shen & Liu, 2020; Shen et al., 2015). This method allows precise recovery of the distinct deformation patterns around the creeping fault zones, as illustrated in Figure 4a and profiles *A*–*A*′, *J*–*J*′ in Figure 5a and *Q*–*Q*′ in Figure 5b.

We estimate fault creep rates by calculating the differential velocity between two cells located on opposite sides of the fault, with the fault-occupied cell in the middle. Figure 6 shows the calculated surface creep rates along fault segments, with the inset figures displaying both along-strike and vertical components in detail. Transects of velocity components showing creep across faults are illustrated in Figure S8 in Supporting Information S1. Significant surface creep is detected along the central California segment of the SAF, where rates reach 23–27 mm/yr across the creeping section, and up to 20 mm/yr on the southern SJB section of the SAF. Other faults, such as the Imperial and Calaveras faults and the northern SJB section of the SAF, exhibit creep rates exceeding 10 mm/yr. Vertical creep rates are more scattered than horizontal creep, with most segments showing less than 5 mm/yr of vertical movement. Additionally, the majority of vertical creep segments show an uplift on the west side relative to the east.

4.2. Vertical Deformation Field

Figure 4b presents the vertical velocity field solution for California and western Nevada. Unlike the horizontal velocity field, where GNSS data are used in the final step, the vertical velocity solution relies primarily on InSAR data, with the horizontal components constrained jointly by the InSAR data and GNSS horizontal measurements. The exclusion of GNSS vertical data is due to the higher variability and scatter in vertical GNSS measurements, which are more affected by surface and subsurface mass changes linked to non-tectonic processes, such as hydrological variations (e.g., Adams et al., 2022; Argus et al., 2017; Fu et al., 2015; Martens et al., 2024), which are more localized and affected more by temporal variations than for horizontal deformation.

Overall, the vertical solution uncertainties are larger than those of the horizontal components, ranging from 1 mm/yr to as much as 7 mm/yr (Figure 4d). They also exceed the uncertainties in the GNSS-only vertical solution (Figure S2d in Supporting Information S1). The GNSS vertical solution was derived using data that excluded signals influenced by non-tectonic processes, such as hydraulic circulation. As a result, its smaller amplitudes and uncertainties do not capture the full spectrum of vertical deformation, which is better represented in the integrated solution. The distribution of uncertainties in the vertical field also shows distinct spatial patterns. The Mojave Shear Zone, with a low uncertainty of about ∼1 mm/yr, is the best resolved area for vertical deformation. This high-resolution result is partly due to the extensive InSAR data set for the region, starting from ERS observations in 1992. Other well-resolved regions include southern California, from the Los Angeles Basin to the southern SAF

Figure 5. 3-D velocity components along profiles which are normal to the Pacific-North America relative plate motion direction. Locations of the profiles are shown in Figure 4a. (a, b), (c, d), and (e, f) are horizontal components parallel (NW motion positive) and normal (NE motion positive) to the relative plate motion, and vertical component, respectively. Red squares are global navigation satellite system (GNSS) data located within a 0.5° bin centered at the profile, and blue curves are velocity components of the integrated velocity solution. Locations of the GNSS sites for the profiles are shown in Figure S6 in Supporting Information S1. Error bars represent 1-standard deviation (STD). Orange bars mark locations of active faults, whose abbreviations are: BF, Banning fault; BSF, Bartlett Springs fault; BWF, Black Water fault; CF, Calaveras fault; CRF, Camp Rock fault; DVF, Death Valley fault; GVF, Green Valley fault; HF, Hayward fault; IF, Imperial fault; LF, Landers fault; MF, Maacama fault; MLF, Moro Lake fault; OVF, Owens Valley fault; PVF, Panamint Valley fault; RCF, Rogers Creek fault; SAF-Ca, Carrizo Plain segment of SAF; SAF-Co, Coachella Valley segment of SAF; SAF-Cr, creeping segment of SAF in central California; SAF-M, Mojave segment of SAF; SAF-SCM, Santa Cruz Mountains segment of SAF; SAF-SJB; San Juan Bautista segment of SAF; SJF, San Jacinto fault.

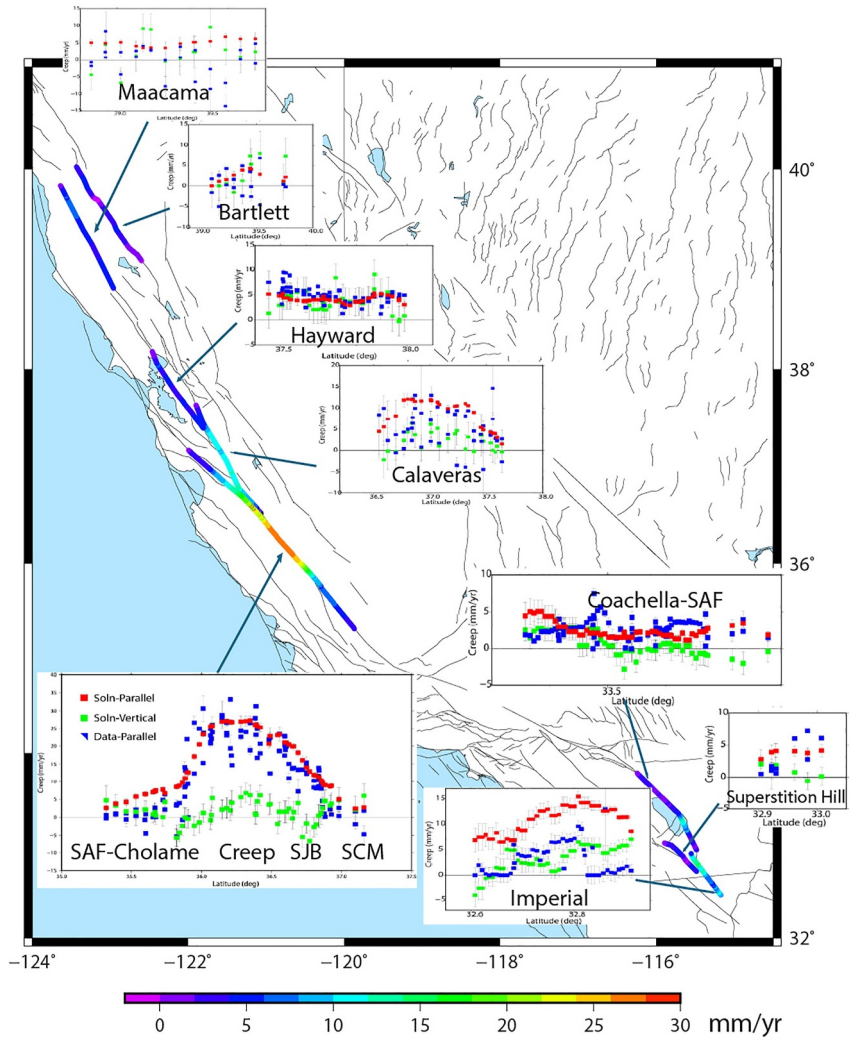

Figure 6. Solution of fault surface creep. The main figure shows map-view of the along-strike component of creep on fault, and the inset figures illustrate the observed and modeled creep on fault segments: the red and green symbols denote the modeled along-strike and vertical components (dextral and west-up positive), and the blue symbol denotes the observed fault-parallel component, respectively. Fault segment name abbreviations: SJB, San Juan Bautista; SCM, Santa Cruz Mountains.

system, where nearly two decades of InSAR data suffice solution with vertical uncertainties of around ∼1.5 mm/yr. Vertical deformation is also resolved to ∼1.5–2.0 mm/yr near Pyramid Lake in northwest Nevada and along the WLFS. In central and northern California, vertical velocity uncertainties range from 2 to 5 mm/yr, with the highest uncertainties (∼7 mm/yr) found east of the Lost Hills Thrust in the SJV. Peripheral regions, particularly the northeast, northwest, and southeast corners of the study area, show elevated uncertainties up to 7 mm/yr, likely due to boundary effects in the interpolation. In the subsequent discussion, we will focus on solutions with uncertainties of ∼2 mm/yr or less, or regions where the deformation amplitudes are significantly above their uncertainty levels, to ensure reliable interpretation.

The most prominent vertical deformation in California is the massive subsidence in the SJV, which is greater than 10 mm/yr for most part of the valley. The largest subsidence is located at two "bullseye" areas between 36.8°N–37.2°N and 35.8°N–36.4°N, with the subsidence rate reaching 150–250 mm/yr (Figure 7d). Another area with up to 40 mm/yr subsidence is located at the southern end of the SJV, north of the White Wolf fault (WWF) and southwest of Bakersfield (Figure 7b). The Sacramento Valley also shows substantial subsidence, with more than half of the region subsiding at rates between 10 and 25 mm/yr, particularly in the western valley (Figure 7a). A similar deformation pattern is detected in the Sacramento Delta region, where up to 25 mm/yr of subsidence is

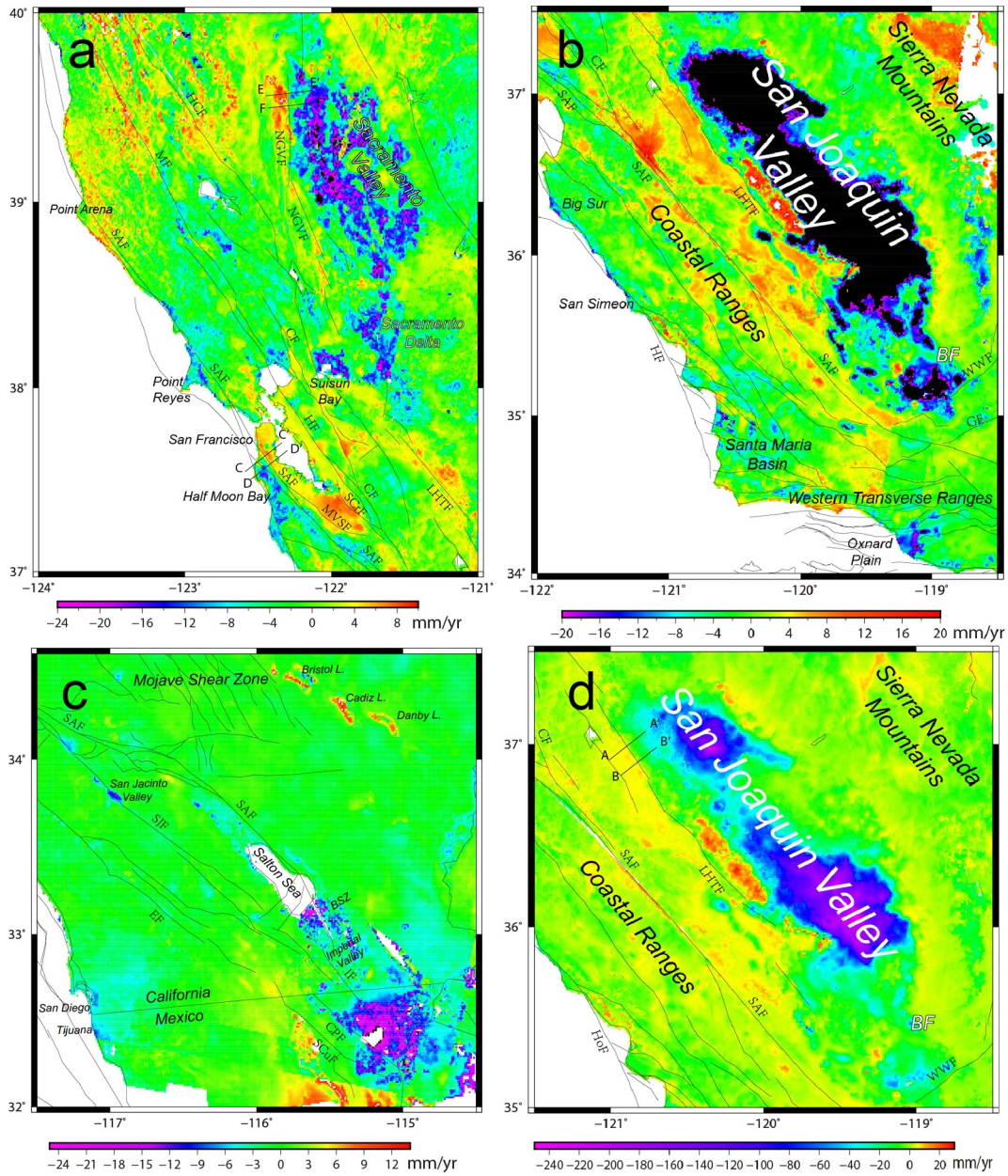

Figure 7. Blow-up view of integrated vertical velocity field in selected regions. (a) Sacramento Valley and San Francisco Bay area. (b) Central coast and Coastal Ranges region. (c) Southeast California region. (d) San Joaquin Valley (SJV) region. Note b and d are largely overlapped due to the spatial closeness of coastal ranges and SJV. Transects across faults are plotted across faults with abrupt offsets: *A*–*A*′ and *B*–*B*′ across the NGVF in panel (a), *C*–*C*′ and *D*–*D*′ across the Peninsula segment of the SAF in panel (a), and *E*–*E*′ and *F*–*F*′ across the LHTF in panel (d), with profile velocity data shown in Figure S10 in Supporting Information S1. Fault and place name abbreviations: BSZ, Brawley Seismic Zone; CF, Calaveras fault; CF-SJB, San Juan Bautista section of CF; CPF, Cerro Prieto fault; EF, Elsinore fault; GF, Garlock fault; HCF, Hunter Creek fault; HF, Hayward fault; HoF, Hosgri fault; IF, Imperial fault; LHTF, Lost Hill Thrust fault; MF, Maacama fault; MVSF, Monte Vista-Shannon fault; NGVF, Northern Great Valley fault; SAF, San Andreas fault; SAF-SJB, San Juan Bautista section of SAF; SCrF, Silver Creek fault; SCuF, Sierra Cucapah fault; SJF, San Jacinto fault; WWF, White Wolf fault.

observed in the eastern part of the Sacramento Delta and around Suisun Bay in the San Francisco Estuary region (Figure 7a).

Considerable subsidence of 6–14 mm/yr is seen at California coastal areas, from Point Reyes (6–10 mm/yr) and Half Moon Bay (6–12 mm/yr) in northern California (Figure 7a and Figure S9 in Supporting Information S1), to

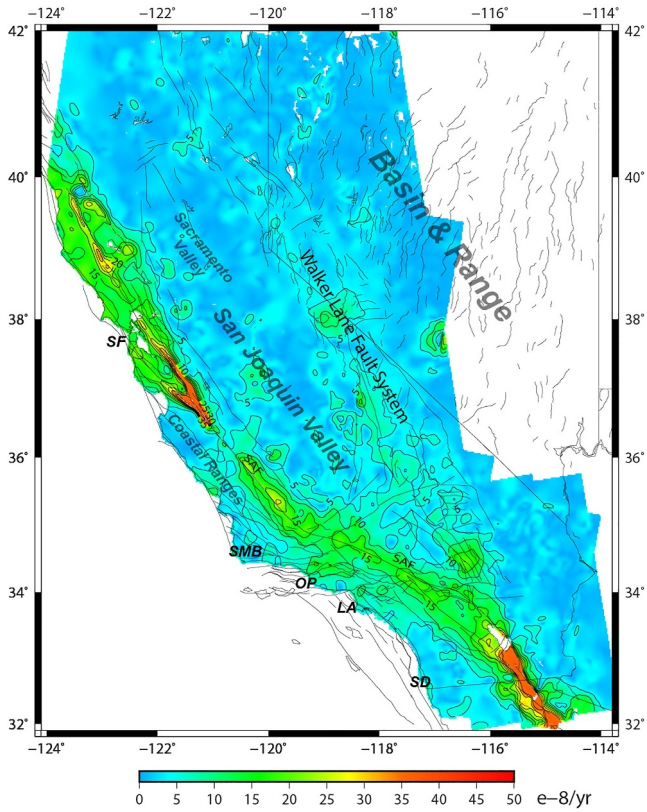

Figure 8. Maximum horizontal shear strain rates derived from integrated velocity solution. LA, Los Angeles; OP, Oxnard Plain; SD, San Diego; SF, San Francisco; SMB, Santa Maria Basin; SAF, San Andreas fault.

San Diego-Tijuana region (2–6 mm/yr) in southern California (Figure 7c and Figure S9 in Supporting Information S1). The highest coastal subsidence rate (8–14 mm/yr) occurs in the Oxnard Plain (OP) (Figure 7b and Figure S9 in Supporting Information S1). The subsidence features are spatially variable and localized. Subsidence of up to 12–18 mm/yr is observed in the Santa Maria basin and Oxnard plain (Figure 7b), and up to 10–25 mm/yr in the region around the southern Imperial and Cerro Prieto faults (Figure 7c).

In contrast with the strong subsidence within the SJV, consistent uplift is also observed surrounding the valley. About 3–5 mm/yr uplift is seen along the west and southwest foothills of the Sierra Nevada Mountains bordering the SJV (Figure 7b). West of the SJV 3–8 mm/yr uplift occurs within parts of the southern Coast Ranges, bounded by the SAF to the west and the Lost Hill-Coalinga thrust fault to the east. The most significant uplift, reaching up to 20 mm/yr, occurs along the western rim of the SJV and east of the Lost Hills Thrust, in a narrow band approximately 20 km wide between ∼120.5°–120.0°W longitude and 36.1°–36.6°N latitude. Uplift rates of up to ∼10 mm/yr are observed at dry lakebeds, including Bristol, Cadiz, and Danby Lakes in the southeastern Mojave Desert, though the precise cause remains uncertain (Figure 7c).

A noticeable deformation feature is the distinct vertical offset observed across tectonically active faults. For instance, there is a ∼4 mm/yr across the Hayward fault (HF), and 1–5 mm/yr across the central section of the Calaveras Fault (CF) (Figure 7a and Figure S8 in Supporting Information S1). Additionally, there are vertical offsets of 5–15 mm/yr across the Peninsula segment of the SAF in the San Francisco Bay area (Figure 7a and Figure S10 in Supporting Information S1), 5–15 mm/yr across the Lost Hills Thrust Fault (LHTF) (Figure 7d and Figure S10 in Supporting Information S1), and 5–20 mm/yr offset across part of the Northern Great Valley Fault (NGVF) west of the Sacramento Valley (Figure 7a and Figure S10 in Supporting Information S1).

4.3. Horizontal Strain Rates

Using the horizontal velocity solution, we compute strain rates by interpolating velocities using the VISR program (Shen & Liu, 2025). Spatial smoothing with a distance constant of 5 km is applied to reduce the impact of short-wavelength and non-tectonic noise (a couple of kilometers in scale) in InSAR data, associated with the residual atmospheric and ionospheric effects. Figure 8 presents the maximum horizontal shear strain rates. The second invariant of strain rates and the dilatation rates are shown in Figure S11 in Supporting Information S1. The second invariant of strain rates is defined as $\tau_{2nd} = (\tau_{ee}^{\ 2} + \tau_{nn}^{\ 2} + 2\,\tau_{en}^{\ 2})^{1/2}$, where τ_{ee} and τ_{nn} are the east and north normal strain rates, and τ_{en} represents east-north shear strain rate.

High shear strain rates are concentrated along the SAFS, with notable variations across its segments. From the Coachella to Cholame segments in southern California, the deformation is broadly distributed, with strain rates peaking at approximately 0.15–0.25 μrad/yr. Similarly, in northern California, broad deformation is observed from the HF to the MF, reaching peak strain rates of ∼0.30–0.35 μrad/yr near the MF. In contrast, the SJB and SCM segments of the SAF, as well as the CF, exhibit more localized strain accumulation, with rates up to 0.4–0.6 μrad/yr. Elevated strain rates are also observed along the southernmost SAFS, particularly across the Brawley Seismic Zone (BSZ) and the Imperial and Cerro Prieto faults, with rates reaching 0.4–0.6 μrad/yr. In central California, little strain accumulation is observed across the creeping segment of the SAF, as strains due to surface creep are excluded from our analysis. The reported strain rates reflect only the elastic component of deformation and can therefore be directly applied in seismic hazard assessments. Strain rates of 0.05–0.10 μrad/yr are recorded across segments of the ECSZ, with peaks reaching up to 0.15 μrad/yr in the southern Mojave Shear Zone. These elevated rates may reflect long-term postseismic deformation following the 1992 Landers and 1999 Hector Mine earthquakes (Liu et al., 2021). A localized zone of high strain rate concentration along the eastern boundary of the study area in southern Nevada could possibly be explained by limitations in InSAR data quality and increased

solution uncertainty, as shown in Figure 4c. Additionally, the bullseye deformation feature in the center of the SJV near ∼120.3°W, 37°N (Figure 8) may be attributed to 3-D bending associated with extreme subsidence at that location.

To further investigate the deformation field, we decompose the strain rate field into three components, namely the shear parallel to, normal parallel to, and normal perpendicular to the Pacific-North America relative plate motion direction. The result shows that: (a) The largest magnitude of strain rates is in the shear parallel component (Figure S12a in Supporting Information S1, as expected), and primarily concentrated along the SAF system, mirroring the total strain rate distribution seen in Figure 8. (b) The normal parallel component (Figure S12b in Supporting Information S1) demonstrates 0.10–0.15 μstrain/yr convergence around Big Bend of the SAF, particularly in the vicinity of WWF, San Gabriel Mountains, and Ventura Basin. Dextral motion around the bifurcation of the SAF near SJB results in up to 0.25 μstrain/yr contraction south of the SCM branch of the SAF and extension southeast of the CF, respectively. Extension up to 0.3 μstrain/yr is also observed within the right-step fault zone between the Cerro Prieto and Imperial faults, close to the California-Mexico border. (c) Deformation rate in the direction normal to relative plate motion is low in general (Figure S12c in Supporting Information S1). The right-step fault zone between the Cerro Prieto and Imperial faults is however experiencing NE-SW contraction at a rate up to 0.3 μstrain/yr, along with NW-SE extension, possibly due to volume conservation. A similar pattern is found in the right-step fault zone between the SJB section of the SAF and the CF, with a strain rate ∼0.15 μstrain/yr. The LHTF zone is experiencing a NE-SW convergence at a rate of ∼0.05–0.1 μstrain/yr. About 0.1–0.2 μstrain convergence is also seen near Mendocino, possibly influenced by eastward bending of the SAF and convergence between the southern section of the Juan De Fuca plate and North America plate.

More smoothed deformation pattern over a larger scale (∼100 km) can be visualized in Figure S13 in Supporting Information S1, which shows the strain rate result interpolated using a smoothing constraint of 20 km. It reveals subtler deformation signals, such as 0.01–0.04 micro-strain/yr northwest-southeast extension in across the central and northern Walker Lane, which is consistent with a geological discovery of normal faulting on the north-trending and basin-bound faults in the basin and range system (Wesnousky et al., 2012).

The central valley and southeast California remain relatively stable with respect to the North America plate, with rotation rates ≤0.01 micro-radian/yr (Figures S12d and S13d in Supporting Information S1). Along most sections of the SAF, rotation rates of 0.2–0.3 μradian/yr correspond to interseismic dextral shear motion. However, rotation intensifies to 0.4–0.6 μradian/yr near the Mendocino triple junction and from the BSZ to CPF, suggesting rapid local rigid-body rotation (Figure S12d in Supporting Information S1).

5. Discussions

5.1. Method Used for GNSS Data Interpolation and Uncertainty Estimation

GNSS and InSAR are two fundamentally different tools for measuring crustal deformation, yet they are highly complementary. However, there is no universally accepted method for recovering a continuous 3D deformation field from these data, and various approaches have been developed to address this challenge. These methods generally fall into two categories, one is about interpolating the discrete GNSS velocity field into a continuous 3D velocity and strain-rate field, and the other is about integrating GNSS and InSAR data to produce a solution with higher precision and spatial resolution than either data set alone. In the following, we describe the unique aspects of our approach compared to those used in previous studies.

Some of the previous interpolation methods model the GNSS velocity field using basic functions such as polynomials or splines (e.g., Haines & Holt, 1993; Hackl et al., 2009; Tape et al., 2009). Other approaches apply elasticity theory (e.g., Haines et al., 2015; Noda & Matsu'ura, 2010; Sandwell & Wessel, 2016), where a concept of elastic tension is introduced to balance resolution robustness with goodness-of-fit. Additionally, linear interpolation methods based on spatial covariance functions have also been developed (e.g., El-Fiky & Kato, 1998; Shen et al., 1996; Goudarzi et al., 2015). While these methods have distinct merits, they also have limitations. Their outcomes often depend heavily on a priori assumptions—such as the polynomial degree, spline scale, or smoothness constraints in spatial covariance functions. Another concern is the uniform treatment of data, without accounting for the variable spatial resolution arising from the uneven distribution of GNSS stations.

More recent approaches aim to better accommodate uneven station spacing. Shen et al. (2015) improved upon their earlier method (Shen et al., 1996) by implementing a spatially varying kernel in the covariance function that

reflects local station density. Kreemer et al. (2018) introduced the Median Estimation of Local Deformation (MELD) method, which uses a weighted median of least squares estimates. Pagani et al. (2021) developed a trans-dimensional Bayesian method that regularizes strain-rate inversion by accounting for grid-spacing uncertainty. Johnson (2024) proposed a variation of the elasticity-based inversion method that uses a triangular mesh with node spacing proportional to GNSS station density. These newer methods provide improved spatial resolution, particularly in regions with irregular station spacing. However, they still rely on certain a priori parameters, which can influence both the results and the uncertainty estimates.

A key distinction of our approach is the rigorous and consistent treatment of GNSS data and interpolation uncertainties throughout the entire process, which is critical for unbiased integration with InSAR data. This begins with re-evaluating GNSS velocity uncertainties. Estimating GNSS velocity uncertainty is notoriously difficult due to spatial and temporal correlations in the data (Santamaría-Gómez et al., 2011). Furthermore, uncertainties derived from time series at individual stations may not fully represent the total uncertainty in site deformation, as they do not capture epistemic uncertainties related to environmental or non-tectonic influences (Shen et al., 2011). For example, some continuous stations in our data set report horizontal velocity uncertainties as low as 0.1 mm/yr —an underestimate if non-tectonic deformation sources are considered.

To address this, we analyze differential velocities of closely spaced station pairs to define minimum uncertainty thresholds. Our composite data set includes dozens of such collocated station pairs, enabling robust statistical analysis. Based on this, we set cutoff uncertainty values at 0.4 mm/yr for horizontal and 0.6 mm/yr for vertical components respectively.

Another consideration is uncertainty estimation of interpolated velocities which is related to the smoothing factor used during interpolation. In this study, a uniform smoothing factor is used for estimating uncertainties, which is different from using a variable smoothing factor to derive the velocity field. This strategy helps prevent bias arised from using inconsistent a priori information during the process. To determine the optimal smoothing factor, we employ an iterative bootstrapping algorithm. The ideal smoothing factor is selected when the median values of the estimated uncertainties match the median of the differences between the interpolated and original velocities at the GNSS sites. The advantage of this method is that it minimizes reliance on a priori assumptions and derives uncertainties primarily from the GNSS velocity data and the spatial configuration of the network.

5.2. Method Used for GNSS and InSAR Data Integration

Various approaches have been developed to integrate GNSS and InSAR data for detailed mapping of surface deformation. These typically involve using GNSS data to constrain or complement the rank–deficient InSAR observations. For example, Tong et al. (2013) developed a method that uses GNSS data to constrain long-wavelength deformation, allowing InSAR to resolve the short-wavelength signals. Wang and Wright (2012) performed a joint inversion of GNSS and InSAR data to estimate a continuous 3D velocity field on a triangular mesh, regularized using Laplacian smoothing—a technique later adopted by Wright et al. (2023). Tymofyeyeva and Fialko (2017) and Xu et al. (2021) instead solved a continuous 3–D velocity field along the SAFS in California, constrained using ascending and descending LOS rate data of InSAR, plus model predicted orientation of horizontal velocities derived from interpolation of GNSS velocity field.

Our method is designed to achieve an optimized solution throughout the entire integration process. We first use all the GNSS and decimated InSAR data to solve for incompatibilities among tracks of InSAR data (offsets and ramps) in a grand least-square regression, and remove their effects from the InSAR LOS rate data. Vertical components of GNSS velocities are included in this step to provide stable long-wavelength constraints on the offset and ramp parameters. Next, we solve for the 3D velocity components at each grid cell using all corrected InSAR data and interpolated GNSS velocity at that cell, via a weighted least squares inversion. The weighting is based on the recalibrated uncertainties of both data types. At this stage, interpolated GNSS vertical velocities are no longer used, as they may not reliably reflect localized non-tectonic vertical deformation.

Unlike some earlier integration methods, our approach relies on minimal a priori assumptions. GNSS and InSAR data are integrated in a single least squares regression to simultaneously solve for all three components of surface velocity. We do not impose external constraints on subsets of the parameters (e.g., fixing north-component velocities or directional priors), as done in some other methods. This design ensures that the final solution is

optimally constrained, though it should be noted that the north-component velocities are still primarily determined by the GNSS input.

Uncertainties in the final solution are propagated through the least squares inversion from the input GNSS and InSAR uncertainties. For most tectonically active regions including the SAFS, Mojave Shear Zone, and WLFS, horizontal velocity uncertainties are approximately 1 mm/yr or less (Figure 4c), similar to those from the interpolated GNSS velocities (Figure S2b in Supporting Information S1), with a few exceptions. Figure S14 in Supporting Information S1 presents the ratio of horizontal velocity uncertainties from the integrated and GNSS-only solutions, $R_\sigma = \sigma_{int}/\sigma_{gnss}$ and σ_{int} and σ_{gnss} denote the uncertainties in the integrated and GNSS solutions respectively. In most areas, $R_\sigma \approx 1$, indicating that the horizontal components of the integrated solution are primarily constrained by GNSS data. However, in some regions such as the northern Mojave Shear Zone, southern Sierra Nevada, southeastern California, and parts of western Nevada R_σ drops below 0.8, where InSAR provides significant additional constraint, likely due to the availability of long-term SAR observations (i.e., ERS and Envisat data from the 1990s–2010s) and sparse GNSS coverage.

Vertical velocity uncertainties in most of the region in the integrated solution are larger than those in the GNSS-only solution, which is expected since interpolated GNSS vertical components are not included in the final integration. Uncertainties are ∼1 mm/yr in the Mojave Shear Zone, the smallest due to long SAR (ERS/Envisat) observation history in the region. For the rest of the ECSZ and WLFS, vertical uncertainties range from ∼1 to 2 mm/yr, and are smaller than those in most other regions outside the ECSZ. The WLFS region benefits from dense Sentinel-1 SAR coverage from 2014 to 2022, while areas to its west in central and northern California are covered by a combination of Sentinel-1 and ALOS-2 data over the same period (Figure 2, Table S1 in Supporting Information S1). Sentinel-1 observations have better precision than ALOS-2, resulting in more accurate vertical velocity estimates and lower uncertainties in the WLFS compared to adjacent regions.

5.3. Comparison of Integrated Velocity Solution With Results of Previous Studies

Crustal deformation in California has been measured extensively over the past three decades using GNSS and InSAR, resulting in the development of numerous deformation models based on a variety of methodological approaches. Recent models based on GNSS data alone include those by Klein et al. (2019), Pagani et al. (2021), Kreemer and Young (2022), Pollitz (2022), Evans (2022), Shen and Bird (2022), Zeng (2022b), and Johnson (2024), and models that integrate both GNSS and InSAR data include those by Tong et al. (2013), Ward et al. (2021), and Xu et al. (2021). While the overall deformation patterns illustrated in these studies generally align with our results, notable differences often arise in the details. These discrepancies may stem from differences in the use of a priori assumptions, such as the choice of polynomial or spline functions, or the design of geometric mesh networks, which complicate direct comparison. Nonetheless, we highlight a few examples that reveal common issues in some of the previous models.

In GNSS-only models, interpolated strain rates sometimes show large dilatational signals in regions without a known source of corresponding tectonic convergence or divergence. For example, Figure 9b of Pagani et al. (2021) showed substantial dilatation across a broad area flanking the central SAF: ∼30–50 nanostrain/yr extension west of the SAF and about the same amount of contraction to the east. Similar patterns also appear across the Bartlett Spring fault and MF up north. Such patterns are inconsistent with the strike-slip dominated tectonic regime of the area. In contrast, our results (Figure S11b in Supporting Information S1) show much smaller, more localized dilatations across the faults, consistent with expected tectonic processes in the region.

In models that integrate GNSS and InSAR data, inaccuracies can arise in the projection of LOS InSAR data into 3-D velocity components. A case in point is shown in Figure 6a of Xu et al. (2021), where an anomalous westward velocity signal is observed along the western edge of the SJV, appearing more than 10 mm/yr slower than both of the adjacent regions to the east and west. This anomaly coincides with a zone of strong subsidence and likely results from imprecise LOS projection of InSAR data. Our solution (Figure S5a in Supporting Information S1), by contrast, does not exhibit this anomaly, demonstrating the robustness of our methodology and the effectiveness of our integration approach.

5.4. Horizontal Deformation Field

Both the San Andreas and Walker Lane fault systems are composed of multiple faults for most of their sections, and the deformation is usually spread over these faults, such as across the San Andreas, San Jacinto, and Elsinore faults in southern California, and the San Andreas, Hayward, and Calaveras faults in northern California, showing no dominant concentration around a single fault. This distributed deformation, potentially due to fault locking within the upper crust, raises ongoing questions about the role of elastic dislocation below locking depth versus viscous deformation in the lower crust and upper mantle (McCaffrey, 2005; Pollitz, 2022). Theoretical models suggest that earthquake induced visco-elastic deformation decays with time and can evolve to a broader region late in an earthquake cycle (e.g., Hearn et al., 2013; Wang et al., 2021). Incorporating earthquake related visco-elastic relaxation into fault-based deformation modeling did provide better interpretation of the data (e.g., Hearn & Thatcher, 2015; Pollitz, 2022; Shen & Bird, 2022; Zeng, 2022b), and this integrated deformation field is consistent with such an interpretation. However, regions with stable blocks, such as the SJV, Sacramento Valley, and southern Mojave Desert east of the Mojave Shear Zone, show little or no deformation (Figures 4, 5a, 5b, 8), indicating that although off-fault deformation is widespread across the boundary zone, it is limited to fault zones rather than extending into stable tectonic blocks.

5.5. Fault Surface Creep

In this study we resolve surface creep rates for various segments of the faults in California, and the results are shown in Figure 6 and Figure S8 in Supporting Information S1. Knowing fault creep rates is important since it is directly related to the degree of fault locking, seismic moment accumulation, and earthquake potential. Fault creep on strands of faults in California has been closely monitored over recent decades using diverse means (Weldon et al., 2013). Johnson et al. (2022) compiled and updated a fault creep data set for California based on these measurements. Here we compare our results against Johnson et al.'s updated data set. Previous creep observations fall into two primary categories: near-fault measurements from creep meters and alignment arrays (e.g., Weldon et al., 2013), and projected horizontal creep from InSAR LOS data (e.g., Xu et al., 2021). We refine the data set based on Johnson et al.'s data quality assessment, excluding data impacted by coseismic and post-seismic deformation and omitting Lidar measurements that showed inconsistencies with other observations (Johnson et al., 2022). Figure 6 illustrates the comparison.

Our results align well with prior observations overall, though some differences are apparent on specific fault segments. For example,: (a) We observe a creep rate of 3–10 mm/yr across the Cholame section of the SAF, whereas previous measurements indicated 0–5 mm/yr. (b) Our results show 10–22 mm/yr across the southern SJB section of the SAF, consistent with previous observations in general (Figure 6). (c) While the along-fault creep pattern of the IF is similar to previous studies, our creep rate estimates (7–15 mm/yr) are consistently higher than earlier measurements (0–9 mm/yr, Figure 6). The contrast is particularly large for the northern part of the fault, amounting 7–13 mm/yr versus 0–2 mm/yr. These discrepancies could stem from several factors. One key difference is the sampling time period, as creep rates may vary over time. Another factor is spatial sampling range. Creepmeter and alignment array data are measured within tens of meters from the fault, while our estimates are based on differential motion between grid cells adjacent to and on opposite side of the fault. With a cell size of $0.02°\text{N} \times 0.02°\text{E}$, the distance between our sampling sites is around 2–3 km. If creep extends beyond a few meters from the fault, our measurements may capture more signal than that of near-fault measurements or short-range InSAR observations (Johnson et al., 2022).

5.6. Vertical Deformation Field

Our result exhibits massive subsidence in the SJV, with subsidence rates reaching 150–250 mm/yr at the center of the valley and up to 40 mm/yr at the southern end of the valley (Figures 7b and 7d). The deformation is derived from InSAR measurements observed by the Sentinel-1 and ALOS-2 satellites from 2015 to 2022, reflecting the impact of aquifer compaction in the semi-confined aquifer layer due to extensive groundwater extraction, exacerbated during recent drought years (Liu et al., 2019). Locations of the bullseye areas are consistent with the subsidence pattern reported in Faunt et al. (2016), detected using InSAR, continuous GNSS, and extensometer during the 2012–2015 drought season.

Our result also reveals substantial subsidence in the Sacramento Valley, with more than half of the region subsiding at rates between 10 and 25 mm/yr, particularly in the western valley (Figure 7a). A similar deformation

pattern is detected in the Sacramento Delta region, where up to 25 mm/yr of subsidence is observed in the eastern part of the Sacramento Delta and around Suisun Bay in the Francisco Estuary region. Our finding is based on Sentinel-1 and ALOS-2 observations in 2015–2022, and the deformation pattern is consistent with a 3–20 mm/yr subsidence reported by Brooks et al. (2012) derived using InSAR from 1995 to 2000, and an averaged subsidence rate of 9.2 mm/yr reported by Bekaert et al. (2019) derived using UAVSAR and GNSS data from 2005 to 2019.

We detect considerable subsidence of 6–14 mm/yr at California coastal areas, from Point Reyes and Half Moon Bay in northern California to San Diego-Tijuana region in southern California (Figure 7 and Figure S9 in Supporting Information S1). The Santa Maria Basin (SMB) and OP were subsiding at rates of 12–18 mm/yr (Figure 7b). Subsidence at lower rates during earlier periods was reported at the coastal areas such as Half Moon Bay (2007–2010) (Shirzaei & Bürgmann, 2018) and SMB and OP (1992–2009) (Hammond et al., 2018) and (2007–2018) (Blackwell et al., 2020), suggesting temporal variation of and possibly heightened subsidence along California coastline. Govorcin et al. (2025) analyzed Sentinel-1 data from 2015 to 2023 to estimate vertical motion along the California coastline, incorporating GNSS constraints. Their results show vertical motion from Point Arena to San Diego that is broadly consistent with ours in terms of overall trends, including uplift around Santa Barbara, Morro Bay, and Point Arena, and subsidence across most other coastal regions (Figure 7 and Figure S9 in Supporting Information S1). However, the amplitudes of their estimated vertical motion are systematically smaller than ours, by roughly a factor of two. For example, they reported subsidence rates of 2–5 mm/yr at Point Reyes compared to our 6–10 mm/yr, 2–7 mm/yr at Half Moon Bay compared to our 6–12 mm/yr, and 1–3 mm/yr in the San Diego region compared to our 2–6 mm/yr. The cause of this discrepancy remains unclear and invites further investigation.

Subsidence of up to ∼10–25 mm/yr is observed in the region around the southern Imperial and Cerro Prieto faults (Figure 7c). This area is part of a pull-apart basin created by a right-step between the IF and CPF, which constitutes part of the boundary between the Pacific and North America plates. This result is consistent with the finding of Xu et al. (2017), which also reported subsidence at the stepover but at a much higher rate (∼40 mm/yr). The heavy agricultural activity in the Imperial Valley has led to substantial groundwater use, which is likely the primary cause of the rapid ground subsidence. Other subsidence regions detected include the BSZ, which is another pull-apart basin in a right-step between the Coachella section of the SAF to the northeast and the IF to the southwest. It is also affected by agricultural activities, and has a subsidence rate of 8–18 mm/yr (Figure 7c). About 8 mm/yr subsidence is identified at the San Jacinto Valley, which is located between two segments of the San Jacinto fault (SJF) with a right step in between, and a dilatational jog created by the dextral motion of the fault system (Park et al., 1995) (Figure 7c).

Our result shows consistent uplift surrounding the SJV, with 3–5 mm/yr uplift along the west and southwest foothills of the Sierra Nevada Mountains and 3–8 mm/yr uplift within the southern Coast Ranges (Figure 7b). Part of the uplift is perhaps caused by the unloading effect of groundwater withdrawal in the SJV (Amos et al., 2014; Borsa et al., 2014; Hammond et al., 2016; Husson et al., 2018), and visco-elastic deformation induced by decades of water depletion in the past may have also contributed (Lundgren et al., 2022). Our estimated uplift rates in the regions surrounding the SJV are based mainly on the InSAR data observed in 2015–2020. About 1–4 mm/yr of uplift was found by analyzing GNSS data of 2004–2010 (Amos et al., 2014; Lundgren et al., 2022) and up to 2 mm/yr of uplift using GNSS data of 1996–2016 (Hammond et al., 2016). The heightened uplift rate (3–8 mm/yr vs. 1–4 mm/yr) may reflect a response to intensified groundwater extraction during recent drought years.

We observe distinct vertical offset across tectonically active faults, such as offsets of 5–20 mm/yr across the NGVF, ∼4 mm/yr across the HF, 1–5 mm/yr across the central section of the CF, 5–15 mm/yr across the peninsula section of the SAF, and 5–15 mm/yr across the LHTF, respectively (Figures 6, 7 and Figures S8, S10 in Supporting Information S1). Some of these fault-related vertical offsets were detected in previous studies (e.g., Chaussard et al., 2014; Xu et al., 2021), but our findings suggest that such deformation is more common near tectonically active faults than previously recognized and sometimes with higher rates than previous estimated. This implies that faults may influence both the pattern and magnitude of vertical deformation. Acting as hydraulic barriers, faults can impede cross-fault fluid flow, thereby modulating vertical responses to seasonal and long-term subsurface water changes driven by climate forcing.

The most significant uplift of up to 20 mm/yr is observed along the western rim of the SJV and east of the Lost Hills Thrust, in a narrow band approximately 20 km wide near the Westside Groundwater Subbasin (Figure 7b) (Kim et al., 2021; Figure 1). Uplift in this area was also detected by Gualandi and Liu (2021) through InSAR data

from 2015 to 2019 and by Xu et al. (2021). Previous studies showed that the uplift motion from 2015 to 2019 was highly nonlinear, with an amplitude of ∼20 mm, and exhibited a temporal pattern that aligned with in situ well water head observations (Gualandi & Liu, 2021). The uplift's location and correlation with coarse-grained materials above the Corcoran clay layer suggest that it is likely a result of the poroelastic response of the shallow unconfined aquifer system to the unusually heavy precipitation during the wetter winter of 2017 (Liu et al., 2019; Gualandi & Liu, 2021).

We detect uplift of up to ∼10 mm/yr at dry lakebeds, including Bristol, Cadiz, and Danby Lakes in the southeastern Mojave Desert, though the precise cause remains uncertain (Figure 7c). Some studies suggest that temporally variable processes, such as soil moisture responses to precipitation and drought, may play a role (Zheng et al., 2022). Additionally, uplift rates of 3–6 mm/yr were identified along a series of normal faults in northwestern Nevada (Figure 4b), likely related to groundwater depletion during drought seasons or to soil moisture changes associated with climate-driven drought conditions.

5.7. Strain Rate Field

In the areas away from major faults in California and western Nevada, strain rates are generally low or near zero. However, analysis of two strain components—normal and parallel to the relative plate motion—reveals an intriguing pattern (Figures S12b and S12c in Supporting Information S1). The normal strain rates in the direction parallel to plate motion exhibit stripe-like bands that run perpendicular to the plate motion, with alternating positive and negative rates spaced tens of kilometers apart. A similar pattern appears in the normal strain rates perpendicular to the plate motion, but here, the stripes are aligned parallel to the plate motion. These patterns were derived using VISR software (Shen et al., 2015) with a 5–km smoothing distance, and they largely disappear when the smoothing distance is increased to 20 km (Figures S13b and S13c in Supporting Information S1). The amplitudes of these alternating strain rates are small, in the range of tens of nano-strain per year, likely due to differential velocities on the sub-millimeter-per-year scale across the bands. The origin of this deformation pattern remains unclear, though it does not appear to be a numerical artifact, as the two strain components display distinct and orthogonal patterns. This observed banding may reflect stress modulation along these directions influenced by gridded crustal material properties, although the underlying mechanisms are yet to be fully understood.

5.8. Seismic Strain Rates

Crustal deformation is closely related to seismic hazard (Bird & Liu, 2007; Petersen et al., 2024; Wesnousky, 1986). Kostrov (1974) first introduced a fundamental relationship linking the average (engineering) elastic strain rate $\dot{\varepsilon}$ over a volume to the seismic moment rate $\dot{M}$ within that volume:

$$\dot{M} = \mu V \dot{\varepsilon} \tag{5}$$

where μ is the shear modulus of the media and V is the volume of the seismogenic material. Variants of the formula have been used for seismic hazard analysis. For instance, in geological studies of fault slip, it can be expressed as:

$$\dot{M} = \mu H L v \tag{6}$$

where H is the seismogenic depth, L the fault length, and v the average fault slip rate in an earthquake cycle (e.g. Working Group on California Earthquake Probabilities, 1995).

The Kostrov formula can also be applied to linking seismic moment rates to geodetically observed surface strain rate (e.g., Ward, 1994; Savage & Simpson, 1997). However, projecting surface observed strain rate tensor into scalar seismic moment rate is not straightforward, and here we adopt the formular proposed by Savage and Simpson (1997):

$$\dot{M} = 2\mu H A \ \mathrm{Max}\left(|\dot{\varepsilon_1}|, |\dot{\varepsilon_2}|, |\dot{\varepsilon_1} + \dot{\varepsilon_2}|\right) \tag{7}$$

Table 1
Areal and Fault Strain Rates Result

Data type and source		Total strain rate (10^4 m^2/yr)
Areal strain rate	P_s, seismic strain using Savage's formula	7.08
	P_{ps}^a, arithmetic sum of shear strain parallel to PM	4.30[a]
	P_{ps}^s, absolute sum of shear strain parallel to PM	4.78
	P_{pn}^a, arithmetic sum of normal strain parallel to PM	−0.03[b]
	P_{pn}^s, absolute sum of normal strain parallel to PM	1.31
	P_{dn}^a, arithmetic sum of normal strain perpendicular to PM	−0.05[b]
	P_{dn}^s, absolute sum of normal strain perpendicular to PM	1.48
Geological fault slip rate	P_{f_geol}, Hatem, Reitman, et al. (2022)	5.65
Geodetic fault slip rate	P_{f_zeng}, Zeng (2022b)	6.10
Geodetic fault slip rate	P_{f_shen}, Shen and Bird (2022)	4.71

Note. PM: relative plate motion direction. [a]Dextral positive. [b]Extension positive.

where $\dot{\varepsilon}_1$ and $\dot{\varepsilon}_2$ are the geodetically derived principal strain rates, and A is the area over which the strain is averaged.

Equations 6 and 7 allow us to associate seismic moments determined from geodetically measured surface deformation to geologically measured slip on tectonic faults. To do so we first evaluate areal strain rates across the study region, defined as:

$$P_s = \int_A S\,(a)\,da \tag{8}$$

where $S = 2\ \mathrm{Max}\ (|\dot{\varepsilon}_1|,; |\dot{\varepsilon}_2|, |\dot{\varepsilon}_1 + \dot{\varepsilon}_2|)$ is the seismic strain rate at location a, and the integration is over the area A of the region. This function can be compared to a fault-based measure defined as:

$$P_f = \int_L v(l)\,dl \tag{9}$$

where v is a fault slip rate, and L is the length of a fault. The integration is over all the faults in the region. We refer to P_s and P_f as areal-strain-related and fault-slip-related "surface potency rate" respectively, since these values are equivalent to Equations 6 and 7 without the common scaling factors of shear modulus μ and seismogenic layer thickness H. Therefore comparing the two quantities of seismic moment accumulation rates is effectively a comparison of P_s corresponding to geodetic strain and P_f corresponding to fault slip. This comparison provides insight into the distribution of on-fault versus off-fault deformation, as P_s encompasses the entire deformation field measured at the Earth's surface, while P_f accounts only for fault-related deformation.

We calculate the integrated areal strain rate using data from this study and compare that with accumulated fault strain rates based on fault slip rate estimates from Hatem, Reitman, et al. (2022), Zeng (2022b), and Shen and Bird (2022) (Figure S15 in Supporting Information S1). The results are presented in Table 1. The integrated seismic strain rate derived using Savage's formula (Equation 8), $P_s = 7.08 \times 10^4$ m^2/yr, reflects contributions from all deformation sources, as well as data error. We also compute the integrated areal strain rates for three strain components $\dot{\varepsilon}_{ps}$ (shear component parallel to relative plate motion direction), $\dot{\varepsilon}_{pn}$ (normal component parallel to plate motion direction), and $\dot{\varepsilon}_{dn}$ (normal component perpendicular to relative plate motion direction):

$$P_x = \int_A \dot{\varepsilon}_x\,(a)\,da \tag{10}$$

where $\dot{\varepsilon}_x = 2\ \dot{\varepsilon}_{ps}$, $\dot{\varepsilon}_{pn}$, and $\dot{\varepsilon}_{dn}$ and $P_x = P_{ps}$, P_{pn}, and P_{dn} respectively. This partitioning of the strain rate field enables a more precise accounting of the strain rate budget and error source and a clearer representation of the deformation field (Figures S12 and S13 in Supporting Information S1).

The strain rate results provide a quantitative assessment of relative contribution of different components to the total areal strain rate budget. Two types of areal integrals of strain rates are calculated: P^a for arithmetic and P^s for scalar (absolute value) sum of the strain rates. The results are: $P^a_{ps} = 4.30 \times 10^4$ m^2/yr, $P^s_{ps} = 4.78 \times 10^4$ m^2/yr, $P^a_{pn} = -3 \times 10^2$ m^2/yr, $P^s_{pn} = 1.31 \times 10^4$ m^2/yr, $P^a_{dn} = -5 \times 10^2$ m^2/yr, and $P^s_{dn} = 1.48 \times 10^4$ m^2/yr, respectively (Table 1). The arithmetic shear strain rate P^a_{ps} is about 12% smaller than the scalar shear strain rate P^s_{ps}, indicating that roughly 6% of the total shear strain in the direction of relative plate motion is sinistral, opposing the dextral shear caused by plate motion. This small amount of reversed deformation is likely due to short-wavelength noise in InSAR data, as indicated by low-level fluctuations of strain rates in regions of low tectonic activity, such as the southeastern Mojave Desert and Central Valley (Figure S12a in Supporting Information S1). For the normal strain component along the plate motion direction, P^a_{pn} is only about 2% of P^s_{pn} in magnitude, suggesting that contractional and extensional strains are nearly balanced, at approximately 51% versus 49%. This symmetry appears to result partly from regional deformation such as contraction around the Big Bend of the SAF and extension in western Nevada (Figure S12b in Supporting Information S1), and partly from the strain rate bands seen in the figure, whose origin remains uncertain. Similarly, examination of the cumulative areal strain rate for the normal component perpendicular to the plate motion, P_{dn}, shows P^a_{dn} to be just 3% of P^s_{dn}, indicating a similar balance between contractional (51.5%) and extensional (48.5%) strains. Again, this component likely reflects mainly the deformation banding observed in Figure S12c in Supporting Information S1, whose origin is yet to be understood.

5.9. Comparison of Areal and Fault-Related Strain Rates

Crustal deformation in California and Nevada has been extensively studied, primarily using geological and geodetic methods. Hatem, Reitman, et al. (2022) summarized field study results and developed a geological deformation model for the 2023 update of the US National Seismic Hazard Model (NSHM2023), incorporating fault geometry and slip rates for over 1,000 faults in the western U.S. Using this geological data set along with a GNSS velocity data set compiled by Zeng (2022a), a group of crustal deformation models were developed for the western U.S. region, employed as the earthquake source models for the NSHM2023 update (Evans, 2022; Pollitz, 2022; Shen & Bird 2022; Zeng, 2022b). Different modeling approaches were taken among these studies, and the results were assigned weights as input for NSHM2023. Here we select estimates of fault slip rates from models of Hatem, Reitman, et al. (2022), Zeng (2022b), and Shen and Bird (2022) to be compared with, as these three models constitute most contributions to NSHM2023 (Petersen et al., 2024).

Figure 9 presents our solution for the velocity component parallel to the relative plate motion direction, along profiles normal to the plate motion direction. Integrated fault slip rates from three models are also plotted, projected to the relative plate motion direction. For all faults, interseismic slip is assumed beneath a 20 km locking depth. The differential motions predicted by these models are largely consistent with the observed motions, including the large dextral motions across the SAFS, which are broadly distributed in southern and northern California but more narrowly distributed along the creeping section of the fault in central California. However, several significant discrepancies are noted:

1. The model predicted differential motions are systematically lower than observed across the Mojave-Walker Lane fault system. As shown in Figure 9, accumulated dextral motion east of the SJV is about 11–13 mm/yr (profiles F–F' to O–O'), and up to 15 mm/yr spanning the southern Basin and Range and Mojave Shear Zone (profiles D–D' and E–E'). Such a deformation pattern is corroborated also by GNSS only measurements of Hammond et al. (2024), which mapped 11–14 mm/yr dextral motion across the central-northern Walker Lane fault and western great basin. All NSHM models however, show differential motion rates much lower across the Mojave Shear Zone and the northern WLFS (8–11 mm/yr lower across profiles E–E' to F–F' and 6–10 mm/yr lower across profiles J–J' to N–N' respectively, Table S3 in Supporting Information S1). The discrepancies are less pronounced across the southern Walker Lane faults (spanning profiles H–H' and I–I'), which are reduced to ∼4–7 mm/yr for Hatem et al.'s and Shen and Bird's models, and virtually none for Zeng's model, due to slip contributions across the Owens Valley, Paramint Valley, and/or Death Valley fault in their solutions.

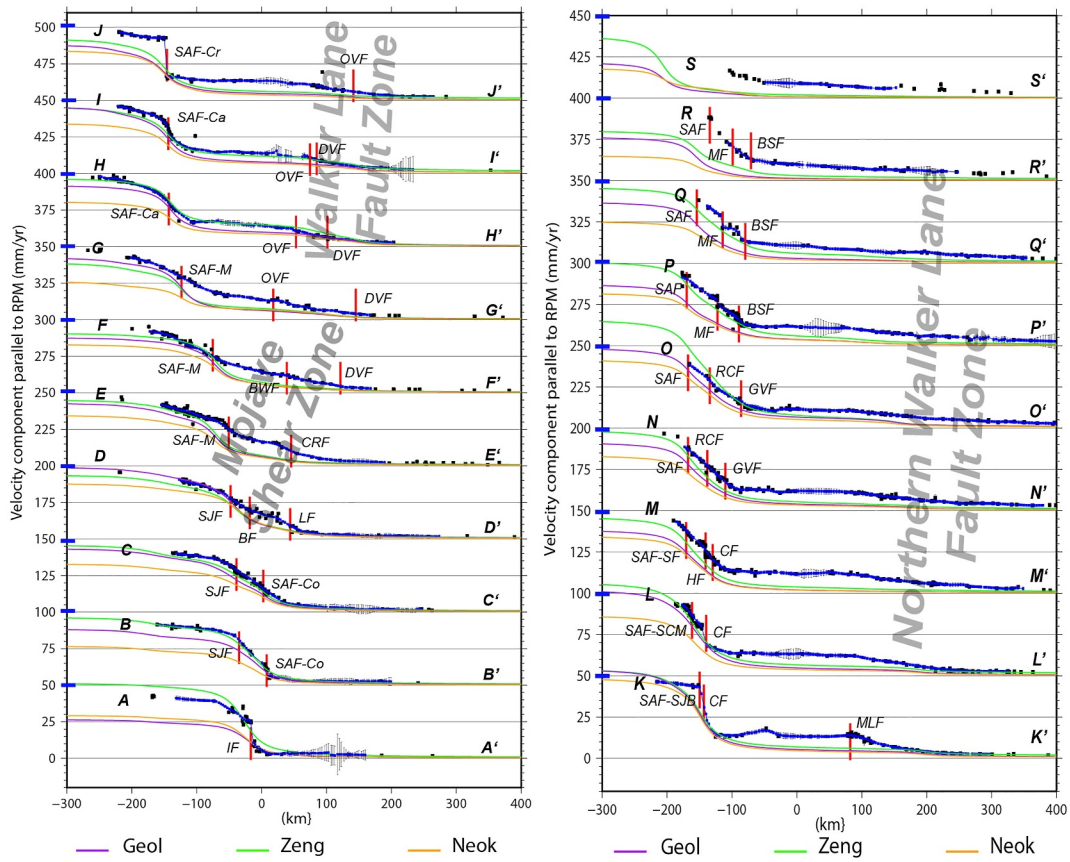

Figure 9. Comparison of model predicted differential motion along profiles normal to the Pacific-North America relative plate motion direction. Locations of the profiles are shown in Figure 4a. The data denote horizontal component parallel to the relative plate motion. Black squares are global navigation satellite system data located within a 0.5° bin centered at the profile, and blue curves are velocity components of the integrated velocity solution. Purple, green, and orange curves mark the model predicted differential motions from Hatem, Reitman, et al. (2022), Zeng (2022b), and Shen and Bird (2022), respectively. Blue bars at the left edge mark model predicted Pacific-North America rigid plate motion. Red vertical bars mark locations of active faults, see Figure 5 caption for their abbreviations.

A smaller discrepancy of ∼4–9 mm/yr is observed in northern Nevada and northeastern California, as shown along profiles *O*–*O*′ to *S*–*S*′. As a result, as noted by Johnson (2024), the NSHM deformation model predicted seismic moment rates (Pollitz et al., 2022) in the Walker Lane and Northern Basin and Range regions are significantly lower than that predicted by the geodetically derived seismic moment rates.

2. Two models, Hatem et al.'s and Zeng's, overestimate the differential motions across certain segments of the SAFS (Table S3 in Supporting Information S1). This includes the Mojave section (∼4 mm/yr overestimate for Zeng's models, profiles *E*–*E*′), the SJB and SCM sections, and the CF (9–10 mm/yr overestimate for Hatem's and 9–12 mm/yr overestimate for Zeng's models, profiles *K*–*K*′ and *L*–*L*′). Zeng's model also overestimates differential motions further north, with discrepancies of 4–18 mm/yr across profiles *M*–*M*′ to *O*–*O*′. However, there are negligible discrepancies across the Mojave section of the SAF for Hatem's model (profiles *E*–*E*′ to *I*–*I*′) and across the Carrizo and creeping sections of the SAF for Zeng's model (profiles *H*–*H*′ to *J*–*J*′).
3. Shen and Bird's model underestimates differential motion across most of the SAF segments in California, with discrepancies of 13 mm/yr or more on segments such as the SJF and the Coachella section of the SAF (profiles *B*–*B*′ and *C*–*C*′), parts of the Mojave and Carrizo sections (profiles *G*–*G*′ and *H*–*H*′), and the SAF, Maacama, and Bartlett Springs faults (profiles *P*–*P*′ to *R*–*R*′) (Table S3 in Supporting Information S1).
4. Hatem's and Shen and Bird's models underestimate the differential motion across the plate boundary fault system south of the California/Mexico border by ∼18–20 mm/yr (profile *A*–*A*′). This discrepancy is attributed to an incomplete model representation of faults near the state border and in Mexico, such as the Cucapah fault.

Postseismic deformation following the 2010 M7.2 El Mayor-Cucapah earthquake is likely responsible for most of this discrepancy in differential motion (Wei et al., 2011; Gualandi et al., 2020).

A possible explanation for the discrepancies between our integrated deformation model and the predicted deformations from geological and geodetic models is that the observed deformation field is broadly distributed, especially across the WLFS. While the geological fault slip model by Hatem, Reitman, et al. (2022) represents a significant improvement over previous models, it still lacked field data to constrain many of the low-slip-rate faults in the Walker Lane and Basin and Range province. If crustal deformation is primarily driven by slip on faults (i.e., discrete fault creep below the upper crust during the interseismic period), the assignment of low slip rate brackets to these faults may have obscured the contributions of a few faults with relatively higher slip rates. Consequently, the geodetic models, which are also partly constrained by the geological model, may be significantly underestimating the total deformation field across the WLFS.

The cause of this distributed deformation may stem from several factors. One interpretation is that the deformation field results from distributed shear in the lower crust, rather than discrete fault slip extending downward from the upper crust. Miller et al. (2024) advocated this view, using a distributed shear model to explain the geodetic velocity field across the northern and central WLFS, and finding that a uniform strain rate model provides a better fit than a fault-based elastic dislocation model. Additionally, the Walker Lane region exhibits higher heat flow and shallower seismogenic depth compared to most of California, implying a more ductile lower crust that can accommodate shear motion more effectively (Blackwell et al., 2006; Zuza & Cao, 2020).

An alternative approach to modeling the deformation field is to incorporate "off-fault" deformation within fault-based deformation models. Shen and Bird (2022), for instance, used a finite element model to explain the deformation field in the western US, attributing it to both fault slip and off-fault deformation. Their findings indicate that off-fault deformation accounts for roughly one-third of the total deformation, aligning closely with the observations in our study. This approach helps explain why their model's predicted differential motions across both fault systems often under-predict observed rates and are generally lower than those of other models, because a portion of the deformation is represented as off-fault deformation, not solely as fault slip.

It is noted that Zeng's model overestimates differential motion across various segments of the SAFS, as shown in profiles E–E', K–K' to L–L', and O–O' (Table S3 in Supporting Information S1). This discrepancy may stem from a compensatory effect, where the model compensates for lower deformation rate estimates across the WLFS and western Nevada. The GNSS velocity field used as model constraints portrays ~50 mm/yr dextral shear across the plate boundary zone in southwest US; as such, underrepresented deformation in the east in Zeng's model might be effectively redistributed westward, resulting in an overestimation of differential motion across the SAFS.

We compare integrated geodetic strain rates across the plate boundary zone with the cumulative strain rates from model-predicted slip on faults. As discussed earlier, the tectonic strains are mainly reflected in P^a_{ps}, the shear component parallel to the relative plate motion direction; and the integrated scalar strains of the other two components P^s_{pn} and P^s_{dn} are mainly attributed to non-tectonic deformation, or at least not related to the slip of the tectonic faults modeled by the geological and geodetic models. The integrated geological fault slip rate of P_{f_geol} (5.65×10^4 m^2/yr) and the integrated geodetic fault slip rate of P_{f_zeng} (6.10×10^4 m^2/yr) are both significantly greater than P^a_{ps} (4.30×10^4 m^2/yr) and P^s_{ps} (4.78×10^4 m^2/yr). Although P_{f_shen} (4.71×10^4 m^2/yr) aligns more closely with P^a_{ps}, this model also includes a significant proportion of off-fault strain—around one-third of the total—which, if added to the strain budget, would bring it to a similar magnitude as the other models. This discrepancy in strain rates may stem from several factors. One possible source is fault slip that deviates from the principal relative plate motion direction, such as on the Garlock and Transverse Ranges faults. However, contributions from these components to the integrated tectonic strains appear minimal, as suggested by the low amplitudes of P^a_{pn} and P^a_{dn} and discussed in Section 5.5. As P^a_{pn} and P^a_{dn} are only ~1% in amplitude comparing to P^a_{ps}, contributions from these components should not be greater than a few percent. Another potential source of discrepancy is the incomplete mapping of deformation across the plate boundary zone within our velocity model, particularly if offshore deformation is underestimated. Offshore deformation however may not be substantial, as a wrench-style deformation extending to the far offshore, suggested by the curvature of onshore data profile, generally aligns with the relative plate motion predicted by the plate motion model (Figure 9), which is calculated using angular velocity of Pacific-North American relative motion from Kreemer et al. (2014).

6. Conclusions

We have developed a method to integrate GNSS and InSAR data to produce a 3–D velocity field. Key elements of the method include: (a) It adopts an optimized approach to interpolate discrete GNSS velocity data points into a continuous velocity field. (b) It takes a pragmatic approach to evaluate uncertainties for InSAR and GNSS measurements as well as interpolated GNSS velocities, to be used as weights for data input. (c) The ramp parameters of multiple tracks of InSAR data are solved through global optimization to minimize systematic biases in the solution. (d) InSAR LOS data are averaged within small grids, and de-ramped InSAR data and interpolated GNSS data are aggregated to solve for 3-D deformation in the grids through least squares regression.

We applied the method to integrate GNSS and InSAR data to solve for 3–D crustal deformation of California and western Nevada. Up to three decades of GNSS data are incorporated, observed in both continuous and campaign modes, and combined with InSAR data acquired over a comparable time span using various satellites and sensors. The spatial-temporal coverage of InSAR data vary over the years, from limited spatial coverage of the ERS/Envisat satellite observations in southern California in 1990s–2010s to the Sentinel-1 and ALOS-2 observations that cover the entire study region from 2014 to the present. The deformation field is well resolved for most of the region, with horizontal component uncertainties averaging around 1 mm/yr or less and vertical uncertainties about 2–3 mm/yr or less, effectively capturing both fault-related tectonic motions and more distributed deformation patterns across the region. Our results show the following:

1. Horizontal crustal deformation at the plate boundary zone in California and western Nevada is dominated by tectonic deformation around the San Andreas and Walker Lane fault systems, with ∼30–40 and ∼8–12 mm/yr dextral shear motion across them, respectively. Most of the deformation field can be interpreted as caused by slip underneath the known tectonic faults in the region, but the residual deformation field is also significant and broadly distributed. This broadly distributed deformation field may be caused by ductile deformation in the substrate of the lithosphere, or anelastic deformation in the upper crust, or both. The mismatch between the observed and fault model interpreted deformation field is particularly significant across the WLFS and western Basin and Range Province, implying that current fault-based models might underestimate seismic moment accumulation and earthquake potential in these regions. This underestimation points to a need for refined seismic hazard assessments that incorporate distributed deformation mechanisms beyond fault slip alone, especially in the areas where tectonic strain may be more diffusely accommodated.
2. Subsidence is widespread in the SJV and Sacramento Valley, with the rates reaching 150–250 and 10–25 mm/yr respectively, likely exacerbated by intensive groundwater extraction. Similarly, areas near the southern Imperial and Cerro Prieto faults show subsidence rates of 10–25 mm/yr. Subsidence reaches up to 12–18 mm/yr in the SMB and OP, possibly influenced by oil and gas extraction. California's coastline experiences significant subsidence at various locations—from Point Reyes and Half Moon Bay down to San Diego-Tijuana, with rates up to 6–14 mm/yr. Many of these coastal subsidence rates are higher than previously documented, suggesting a potential increase in coastal and nearshore impacts.
3. Uplift is occurring in surrounding mountainous regions of the SJV. The Sierra Nevada Mountains and the Southern Coastal Ranges show uplift rates of 3–5 and 3–8 mm/yr, respectively, potentially driven by elastic rebound related to the loss of groundwater in adjacent valley. The complex pattern of subsidence and uplift has implications for regional water management, land use, and infrastructure stability, highlighting the need for ongoing monitoring and adaptive management strategies.
4. Abrupt vertical offsets are observed across tectonically active faults, such as 5–20 mm/yr across the NGVF, 5–15 mm/yr across the LHTF, and 5–15 mm/yr across the peninsula section of the SAF, respectively. The vertical offsets reflect differential subsurface mass changes related to variations in sediment type, hydrogeology, and groundwater movement. It suggests that faults acting as hydraulic barriers, can influence vertical deformation by modulating groundwater circulation associated with dynamic recharge and extraction of groundwater in the underlying aquafer system.

Conflict of Interest

The authors declare no conflicts of interest relevant to this study.

Data Availability Statement

Fortran codes and the input/output files to compute deformation field (gic3d.f) and velocity interpolation (visr_n.f) at California and western Nevada are archived at (Shen & Liu, 2025) and are freely accessible. No registration is required.

Data and Software Citation: The primary GNSS velocity data are from the NASA-Scripps MEaSUREs project (Bock et al., 2025). Additional GNSS velocity data are from a compilation of Zeng (2022a). Geological fault data are from Hatem, Collett, et al. (2022), and can be accessed at Hatem (2023). We thank ESA for its open data policy for ERS, Envisat, and Sentinel-1 data (CDSE, 2025) and JAXA for making ALOS-2 ScanSAR data (ALOS, 2025) publicly available. The GMT software (Wessel et al., 2019) was used for graphics of the study.

Acknowledgments
We would like to thank Roland Burgmann, Yuehua Zeng, Jeremy Maurer, associate editor Lujia Feng, and an anonymous reviewer for their insightful and constructive comments. Part of the work was carried out at the Jet Propulsion Laboratory, California Institute of Technology, under a contract with the National Aeronautics and Space Administration (80NM0018D0004 and 80NM0018F0591), and supported by NASA Earth Surface and Interior program. This research was also supported by the Statewide California Earthquake Center (SCEC) (Contribution No.14121). SCEC is funded by NSF Cooperative Agreement EAR-2225216 and USGS Cooperative Agreement G24AC00072. Additional support was provided by NASA Grant 80NSSC19K0739.

References

Adams, K. H., Reager, J. T., Rosen, P., Wiese, D., Farr, T., Rao, S., et al. (2022). Remote sensing of groundwater: Current capabilities and future directions. *Water Resources Research*, *58*(10), e2022WR032219. https://doi.org/10.1029/2022WR032219

ALOS. (2025). ALOS-2 ScanSAR data [Dataset]. *ALOS*. Retrieved from https://www.eorc.jaxa.jp/ALOS/en/alos-2/a2_about_e.htm

Altamimi, Z., Métivier, L., Rebischung, P., Rouby, H., & Collilieux, X. (2017). ITRF2014 plate motion model. *Geophysical Journal International*, *209*(3), 1906–1912. https://doi.org/10.1093/gji/ggx136

Amos, C. B., Audet, P., Hammond, W. C., Bürgmann, R., Johanson, I. A., & Blewitt, G. (2014). Uplift and seismicity driven by groundwater depletion in central California. *Nature*, *509*(7501), 483–486. https://doi.org/10.1038/nature13275

Argus, D. F., Landerer, F. W., Wiese, D. N., Martens, H. R., Fu, Y., Famiglietti, J. S., et al. (2017). Sustained water loss in California's Mountain ranges during severe drought from 2012 to 2015 inferred from GPS. *Journal of Geophysical Research: Solid Earth*, *122*(12), 10559–10585. https://doi.org/10.1002/2017JB014424

Bekaert, D. P., Jones, C. E., An, K., & Huang, M. H. (2019). Exploiting UAVSAR for a comprehensive analysis of subsidence in the Sacramento Delta. *Remote Sensing of Environment*, *220*, 124–134. https://doi.org/10.1016/j.rse.2018.10.023

Bird, P. (2009). Long-term fault slip rates, distributed deformation rates, and forecast of seismicity in the Western United States from joint fitting of community geologic, geodetic, and stress direction data sets. *Journal of Geophysical Research*, *114*(B11). https://doi.org/10.1029/2009jb006317

Bird, P., & Liu, Z. (2007). Seismic hazard inferred from tectonics: California, Seism. *Research Letters*, *78*(1), 37–48. https://doi.org/10.1785/gssrl.78.1.37

Blackwell, D. D., Negraru, P. T., & Richards, M. C. (2006). Assessment of the enhanced geothermal system resource base of the United States. *Natural Resources Research*, *15*(4), 283–308. https://doi.org/10.1007/s11053-007-9028-7

Blackwell, E., Shirzaei, M., Ojha, C., & Werth, S. (2020). Tracking California's sinking coast from space: Implications for relative sea-level rise. *Science Advances*, *6*(31), eaba4551. https://doi.org/10.1126/sciadv.aba4551

Blewitt, G., Kreemer, C., Hammond, W. C., & Gazeaux, J. (2016). MIDAS robust trend estimator for accurate GPS station velocities without step detection. *Journal of Geophysical Research*, *121*(3), 2054–2068. https://doi.org/10.1002/2015JB012552

Bock, Y., Moore, A. W., Argus, D., Fang, P., Golriz, D., Guns, K., et al. (2021). Extended Solid Earth Science ESDR System (ES3): Algorithm theoretical basis document. NASA MEaSUREs project, #NNH17ZDA001N. Retrieved from http://garner.ucsd.edu/pub/measuresESESES_products/ATBD/ESESES-ATBD.pdf

Bock, Y., Moore, W., Argus, D. F., Fang, P., Jiang, S., Kedar, S., et al. (2025). MEaSUREs project ITRF2014 velocities [Dataset]. Retrieved from http://sopac-csrc.ucsd.edu/index.php/velocities/

Borsa, A. A., Agnew, D. C., & Cayan, D. R. (2014). Ongoing drought-induced uplift in the western United States. *Science*, *345*(6204), 1587–1590. https://doi.org/10.1126/science.1260279

Brooks, B. A., Bawden, G., Manjunath, D., Werner, C., Knowles, N., Foster, J., et al. (2012). Contemporaneous subsidence and levee overtopping potential, Sacramento-San Joaquin Delta, California. *San Francisco Estuary and Watershed Science*, *10*(1). https://doi.org/10.15447/sfews.2012v10iss1art4

Bürgmann, R., Hilley, G., Ferretti, A., & Novali, F. (2006). Resolving vertical tectonics in the San Francisco Bay area from permanent scatterer InSAR and GPS analysis. *Geology*, *34*(3), 221–224. https://doi.org/10.1130/G22064.1

CDSE. (2025). ESA Sentinel-1 copernicus data space ecosystem [Dataset]. *CDSE*. Retrieved from https://dataspace.copernicus.eu/explore-data/data-collections/sentinel-data/sentinel-1

Chaussard, E., Bürgmann, R., Shirzaei, M., Fielding, E. J., & Baker, B. (2014). Predictability of hydraulic head changes and characterization of aquifer-system and fault properties from InSAR-derived ground deformation. *Journal of Geophysical Research: Solid Earth*, *119*, 6572–6590. https://doi.org/10.1002/2014JB01126

d'Alessio, M. A., Johanson, I. A., Bürgmann, R., Schmidt, D. A., & Murray, M. H. (2005). Slicing up the San Francisco Bay area: Block kinematics and fault slip rates from GPS-derived surface velocities. *Journal of Geophysical Research*, *110*(B6). https://doi.org/10.1029/2004jb003496

Dixon, T. H., Miller, M., Farina, F., Wang, H., & Johnson, D. (2000). Present-day motion of the Sierra Nevada block and some tectonic implications for the Basin and Range province, North American Cordillera. *Tectonics*, *19*(1), 1–24. https://doi.org/10.1029/1998tc001088

Efron, B., & Stein, C. (1981). The jackknife estimate of variance. *Annals of Statistics*, *9*(3), 586–596. https://doi.org/10.1214/aos/1176345462

El-Fiky, G. S., & Kato, T. (1998). Continuous distribution of the horizontal strain in the Tohoku district, Japan, predicted by least-squares collocation. *Journal of Geodynamics*, *27*(2), 213–236. https://doi.org/10.1016/S0264-3707(98)00006-4

Evans, E. L. (2022). A dense block model representing western continental United States deformation for the 2023 update to the National Seismic Hazard Model. *Seismological Society of America*, *93*(6), 3024–3036. https://doi.org/10.1785/0220220141

Fang, J., Wright, T. J., Johnson, K. M., Ou, Q., Styron, R., Craig, T. J., et al. (2024). Strain partitioning in the Southeastern Tibetan Plateau from kinematic modeling of high-resolution Sentinel-1 InSAR and GNSS. *Geophysical Research Letters*, *51*(19), e2024GL111199. https://doi.org/10.1029/2024gl111199

Fattahi, H., Agram, P., & Simons, M. (2017). A network-based enhanced spectral diversity approach for TOPS time-series analysis. *IEEE Transactions on Geoscience and Remote Sensing*, *55*(2), 777–786. https://doi.org/10.1109/TGRS.2016.2614925

Fattahi, H., & Amelung, F. (2014). InSAR uncertainty due to orbital errors. *Geophysical Journal International*, *199*(1), 549–560. https://doi.org/10.1093/gji/ggu276

Faunt, C. C., Sneed, M., Traum, J., & Brandt, J. T. (2016). Water availability and land subsidence in the Central Valley, California, USA. *Hydrogeology Journal*, *24*(3), 675–684. https://doi.org/10.1007/s10040-015-1339-x

Feigl, K. L., Agnew, D. C., Bock, Y., Dong, D., Donnellan, A., Hager, B. H., et al. (1993). Space geodetic measurement of crustal deformation in central and southern California, 1984–1992. *Journal of Geophysical Research*, *98*(B12), 21677–21712. https://doi.org/10.1029/93jb02405

Fialko, Y. (2006). Interseismic strain accumulation and the earthquake potential on the southern San Andreas fault system. *Nature*, *441*(7096), 968–971. https://doi.org/10.1038/nature04797

Fu, Y., Argus, D. F., & Landerer, F. W. (2015). GPS as an independent measurement to estimate terrestrial water storage variations in Washington and Oregon. *Journal of Geophysical Research: Solid Earth*, *120*(1), 552–566. https://doi.org/10.1002/2014JB011415

Goudarzi, M. A., Cocard, M., & Santerre, R. (2015). GeoStrain: An open source software for calculating crustal strain rates. *Computers and Geosciences*, *82*, 1–12. https://doi.org/10.1016/j.cageo.2015.05.007

Govorcin, M., Bekaert, D. P., Hamlington, B. D., Sangha, S. S., & Sweet, W. (2025). Variable vertical land motion and its impacts on sea level rise projections. *Science Advances*, *11*(5), eads8163. https://doi.org/10.1126/sciadv.ads8163

Gualandi, A., & Liu, Z. (2021). Variational Bayesian independent component analysis for InSAR displacement time-series with application to central California, USA. *Journal of Geophysical Research: Solid Earth*, *126*(4), e2020JB020845. https://doi.org/10.1029/2020JB020845

Gualandi, A., Liu, Z., & Rollins, C. (2020). Post-large earthquake seismic activities mediated by aseismic deformation processes. *Earth and Planetary Science Letters*, *530*, 115870. https://doi.org/10.1016/j.epsl.2019.115870

Hackl, M., Malservisi, R., & Wdowinski, S. (2009). Strain rate patterns from dense GPS networks. *Natural Hazards and Earth System Sciences*, *9*(4), 1177–1187. https://doi.org/10.5194/nhess-9-1177-2009

Haines, A. J., Dimitrova, L. L., Wallace, L. M., & Williams, C. A. (2015). Introduction to the vertical derivatives of horizontal stress (VDoHS) rates. In A. J. Haines, L. L. Dimitrova, L. M. Wallace, & C. A. Williams (Eds.), *Enhanced surface imaging of crustal deformation: Obtaining tectonic force fields using GPS data. SpringerBriefs in Earth Sciences* (pp. 9–18). Springer International Publishing. https://doi.org/10.1007/978-3-319-21578-5_2

Haines, A. J., & Holt, W. E. (1993). A procedure to obtain the complete horizontal motions within zones of distributed deformation from the inversion of strain rate data. *Journal of Geophysical Research*, *98*(B7), 12057–12082. https://doi.org/10.1029/93jb00892

Hamilton, W., & Myers, W. B. (1966). Cenozoic tectonics of the western United States. *Reviews of Geophysics*, *4*(4), 509–549. https://doi.org/10.1029/rg004i004p00509

Hammond, W. C., Blewitt, G., & Kreemer, C. (2011). Block modeling of crustal deformation of the northern Walker Lane and basin and range from GPS velocities. *Journal of Geophysical Research*, *116*(B4), B04402. https://doi.org/10.1029/2010jb007817

Hammond, W. C., Blewitt, G., & Kreemer, C. (2016). GPS imaging of vertical land motion in California and Nevada: Implications for Sierra Nevada uplift. *Journal of Geophysical Research: Solid Earth*, *121*(10), 7681–7703. https://doi.org/10.1002/2016JB013458

Hammond, W. C., Burgette, R. J., Johnson, K. M., & Blewitt, G. (2018). Uplift of the western transverse ranges and Ventura area of Southern California: A four-technique geodetic study combining GPS, InSAR, leveling, and tide gauges. *Journal of Geophysical Research: Solid Earth*, *123*(1), 836–858. https://doi.org/10.1002/2017jb014499

Hammond, W. C., Kreemer, C., & Blewitt, G. (2024). Robust imaging of fault slip rates in the Walker Lane and western Great Basin from GPS data using a multi-block model approach. *Journal of Geophysical Research: Solid Earth*, *129*(3), e2023JB028044. https://doi.org/10.1029/2023jb028044

Hatem, A. E. (2023). Earthquake geology inputs for the 2023 National Seismic Hazard Model (conterminous U.S.) [Dataset]. Retrieved from https://www.sciencebase.gov/catalog/item/5fe1149ad34e30b9123f0160

Hatem, A. E., Collett, C. M., Briggs, R. W., Gold, R. D., Angster, S. J., Field, E. H., et al. (2022). Simplifying complex fault data for systems-level analysis: Earthquake geology inputs for US NSHM 2023. *Scientific Data*, *9*(1), 506. https://doi.org/10.1038/s41597-022-01609-7

Hatem, A. E., Reitman, N. G., Briggs, R. W., Gold, R. D., Thompson Jobe, J. A., & Burgette, R. J. (2022). Western US geologic deformation model for use in the US National Seismic Hazard Model 2023. *Seismological Society of America*, *93*(6), 3053–3067. https://doi.org/10.1785/0220220154

Hearn, E. H., Pollitz, F. F., Thatcher, W. R., & Onishi, C. T. (2013). How do "ghost transients" from past earthquakes affect GPS slip rate estimates on southern California faults? *Geochemistry, Geophysics, Geosystems*, *14*(4), 828–838. https://doi.org/10.1002/ggge.20080

Hearn, E. H., & Thatcher, W. R. (2015). Reconciling viscoelastic models of postseismic and interseismic deformation: Effects of viscous shear zones and finite length ruptures. *Journal of Geophysical Research: Solid Earth*, *120*(4), 2794–2819. https://doi.org/10.1002/2014jb011361

Husson, L., Bodin, T., Spada, G., Choblet, G., & Kreemer, C. (2018). Bayesian surface reconstruction of geodetic uplift rates: Mapping the global fingerprint of glacial isostatic adjustment. *Journal of Geodynamics*, *122*, 25–40. https://doi.org/10.1016/j.jog.2018.10.002

Johnson, K. M. (2024). Disagreements in geodetically inferred strain rates in the western US with stress orientations and geologic moment rates. *Journal of Geophysical Research: Solid Earth*, *129*(4), e2023JB027472. https://doi.org/10.1029/2023jb027472

Johnson, K. M., Murray, J. R., & Wespestad, C. (2022). Creep rate models for the 2023 US National Seismic Hazard Model: Physically constrained inversions for the distribution of creep on California faults. *Seismological Society of America*, *93*(6), 3151–3169. https://doi.org/10.1785/0220220186

Kim, K. H., Liu, Z., Rodell, M., Beaudoing, H. K., Massoud, E., Kitchens, J., et al. (2021). An evaluation of remotely sensed and in situ data sufficiency for SGMA-scale groundwater studies in the Central Valley, California. *Journal of the American Water Resources Association*, *57*(5), 664–674. https://doi.org/10.1111/1752-1688.12898

Klein, E., Bock, Y., Xu, X., Sandwell, D. T., Golriz, D., Fang, P., & Su, L. (2019). Transient deformation in California from two decades of GPS displacements: Implications for a three-dimensional kinematic reference frame. *Journal of Geophysical Research: Solid Earth*, *124*(11), 12189–12223. https://doi.org/10.1029/2018jb017201

Kostrov, V. V. (1974). Seismic moment and energy of earthquakes, and the seismic flow of rock. *Izvstiya Academic Science USSR. Physics of Solid Earth*, *1*, 23–44.

Kreemer, C., Blewitt, G., & Klein, E. C. (2014). A geodetic plate motion and Global Strain Rate Model. *Geochemistry, Geophysics, Geosystems*, *15*(10), 3849–3889. https://doi.org/10.1002/2014gc005407

Kreemer, C., Hammond, W. C., & Blewitt, G. (2018). A robust estimation of the 3-D intraplate deformation of the North American plate from GPS. *Journal of Geophysical Research: Solid Earth*, *123*(5), 4388–4412. https://doi.org/10.1029/2017JB015257

Kreemer, C., & Young, Z. M. (2022). Crustal strain rates in the western United States and their relationship with earthquake rates. *Seismological Society of America*, *93*(6), 2990–3008. https://doi.org/10.1785/0220220153

Liang, C., & Fielding, E. J. (2017a). Interferometry with ALOS-2 full-aperture ScanSAR data. *IEEE Transactions on Geoscience and Remote Sensing*, *55*(5), 2739–2750. https://doi.org/10.1109/TGRS.2017.2653190

Liang, C., & Fielding, E. J. (2017b). Measuring azimuth deformation with L-Band ALOS-2 ScanSAR interferometry. *IEEE Transactions on Geoscience and Remote Sensing*, *55*(5), 2725–2738. https://doi.org/10.1109/tgrs.2017.2653186

Liang, C., Liu, Z., Fielding, E., & Burgmann, R. (2018). InSAR time series analysis of L-band wide-swath SAR data acquired by ALOS-2. *IEEE Transactions on Geoscience and Remote Sensing*, *56*(8), 4492–4506. https://doi.org/10.1109/TGRS.2018.2821150

Lisowski, M., Savage, J. C., & Prescott, W. H. (1991). The velocity field along the San Andreas fault in central and southern California. *Journal of Geophysical Research*, *96*(B5), 8369–8389. https://doi.org/10.1029/91jb00199

Liu, S., Shen, Z. K., Burgmann, R., & Jonsson, S. (2021). Thin crème brûlée rheological structure for the Eastern California Shear Zone. *Geology*, *49*(2), 216–221. https://doi.org/10.1130/G47729.1

Liu, Z., Liu, P. W., Massoud, E., Farr, T. G., Lundgren, P., & Famiglietti, J. S. (2019). Monitoring groundwater change in California's Central Valley using Sentinel-1 and GRACE observations. *Geosciences*, *9*(10), 436. https://doi.org/10.3390/geosciences9100436

Liu, Z., Lundgren, P., & Shen, Z. (2014). Improved imaging of Southern California crustal deformation using InSAR and GPS, SCEC annual meeting. SCEC contribution# 2038.

Lundgren, P., Liu, Z., & Ali, S. T. (2022). San Andreas fault stress change due to groundwater withdrawal in California's Central Valley, 1860–2010. *Geophysical Research Letters*, *49*(3), e2021GL095975.

Marinkovic, P., & Larsen, Y. (2013). Consequences of long-term ASAR local oscillator frequency decay - An empirical study of 10 years of data, ESA living planet symposium, Edinburgh, UK.

Martens, H. R., Lau, N., Swarr, M. J., Argus, D. F., Cao, Q., Young, Z. M., et al. (2024). GNSS geodesy quantifies water-storage gains and drought improvements in California spurred by atmospheric rivers. *Geophysical Research Letters*, *51*(13), e2023GL107721. https://doi.org/10.1029/2023GL107721

McCaffrey, R. (2005). Block kinematics of the Pacific–North America plate boundary in the southwestern United States from inversion of GPS, seismological, and geologic data. *Journal of Geophysical Research*, *110*(B7). https://doi.org/10.1029/2004jb003307

Miller, N. M., Kreemer, C., Hammond, W. C., & Blewitt, G. (2024). Geodetic evidence for distributed shear below the brittle crust of the Walker Lane, western United States. *Journal of Geophysical Research: Solid Earth*, *129*(9), e2024JB028848. https://doi.org/10.1029/2024jb028848

Neely, W. R., Borsa, A. A., Burney, J. A., Levy, M. C., Silverii, F., & Sneed, M. (2021). Characterization of groundwater recharge and flow in California's San Joaquin Valley from InSAR-observed surface deformation. *Water Resources Research*, *57*(4), e2020WR028451. https://doi.org/10.1029/2020wr028451

Noda, A., & Matsu'ura, M. (2010). Physics-based GPS data inversion to estimate three-dimensional elastic and inelastic strain fields. *Geophysical Journal International*, *182*(2), 513–530. https://doi.org/10.1111/j.1365-246X.2010.04611.x

Pagani, C., Bodin, T., Métois, M., & Lasserre, C. (2021). Bayesian estimation of surface strain rates from global navigation satellite system measurements: Application to the southwestern United States. *Journal of Geophysical Research: Solid Earth*, *126*(6), e2021JB021905. https://doi.org/10.1029/2021JB021905

Park, S. K., Pendergraft, D., Stephenson, W. J., Shedlock, K. M., & Lee, T. C. (1995). Delineation of intrabasin structure in a dilational jog of the San Jacinto fault zone, southern California. *Journal of Geophysical Research*, *100*(B1), 691–702. https://doi.org/10.1029/94jb02469

Petersen, M. D., Shumway, A. M., Powers, P. M., Field, E. H., Moschetti, M. P., Jaiswal, K. S., et al. (2024). The 2023 US 50-State National Seismic Hazard Model: Overview and implications. *Earthquake Spectra*, *40*(1), 5–88. https://doi.org/10.1177/87552930231215428

Pollitz, F. F. (2022). Viscoelastic fault-based model of crustal deformation for the 2023 update to the US National Seismic Hazard Model. *Seismological Society of America*, *93*(6), 3087–3099. https://doi.org/10.1785/0220220137

Pollitz, F. F., Evans, E. L., Field, E. H., Hatem, A. E., Hearn, E. H., Johnson, K., et al. (2022). Western US deformation models for the 2023 update to the US National Seismic Hazard Model. *Seismological Research Letters*, *93*(6), 3068–3086. https://doi.org/10.1785/0220220143

Rosen, P. A., Gurrola, E., Sacco, G. F., & Zebker, H. (2012). The InSAR scientific computing environment. In *EUSAR 2012; 9th European conference on synthetic aperture radar* (pp. 730–733). VDE.

Samsonov, S. (2010). Topographic correction for ALOS PALSAR interferometry. *IEEE Transactions on Geoscience and Remote Sensing*, *48*(7), 3020–3027. https://doi.org/10.1109/tgrs.2010.2043739

Sandwell, D. T., & Wessel, P. (2016). Interpolation of 2-D vector data using constraints from elasticity. *Geophysical Research Letters*, *43*(20), 10703–10709. https://doi.org/10.1002/2016GL070340

Sansosti, E., Casu, F., Manzo, M., & Lanari, R. (2010). Space-borne radar interferometry techniques for the generation of deformation time series: An advanced tool for Earth's surface displacement analysis. *Geophysical Research Letters*, *37*(20), L20305. https://doi.org/10.1029/2010GL044379

Santamaría-Gómez, A., Bouin, M. N., Collilieux, X., & Wöppelmann, G. (2011). Correlated errors in GPS position time series: Implications for velocity estimates. *Journal of Geophysical Research*, *116*(B1), B01405. https://doi.org/10.1029/2010jb007701

Savage, J. C., & Simpson, R. W. (1997). Surface strain accumulation and the seismic moment tensor. *Bulletin of the Seismological Society of America*, *87*(5), 1345–1353. https://doi.org/10.1785/bssa0870051345

Shen, Z.-K. (2017). Updating Western US crustal motion map, final technical report of the USGS earthquake hazards program assistance awards. Retrieved from https://earthquake.usgs.gov/cfusion/external_grants/reports/G16AP00059.pdf

Shen, Z.-K., & Bird, P. (2022). Neokinema deformation model for the 2023 update to the US National Seismic Hazard Model. *Seismological Society of America*, *93*(6), 3037–3052. https://doi.org/10.1785/0220220179

Shen, Z.-K., Jackson, D. D., & Ge, B. X. (1996). Crustal deformation across and beyond the Los Angeles basin from geodetic measurements. *Journal of Geophysical Research*, *101*(B12), 27957–27980. https://doi.org/10.1029/96jb02544

Shen, Z.-K., King, R., Agnew, D., Wang, M., Herring, T. A., Dong, D., & Fang, P. (2011). A unified analysis of crustal motion in Southern California, 1970-2004: The SCEC crustal motion map. *Journal of Geophysical Research*, *116*(B11), B11402. https://doi.org/10.1029/2011JB008549

Shen, Z.-K., & Liu, Z. (2020). Integration of GPS and InSAR data for resolving 3-Dimensional crustal deformation. *Earth and Space Science*, *7*(4), e2019EA001036. https://doi.org/10.1029/2019ea001036

Shen, Z.-K., & Liu, Z. (2025). Software package including the fortran code gic3d.f and the input and output files for the 3-D velocity field production, and the fortran code visr_n.f and the input and output files for the horizontal strain rate interpolation [Dataset] [Software]. *Harvard Dataverse*. https://doi.org/10.7910/DVN/UV8M8L

Shen, Z.-K., Wang, M., Zeng, Y., & Wang, F. (2015). Strain determination using spatially discrete geodetic data. *Bulletin of the Seismological Society of America*, *105*(4), 2117–2127. https://doi.org/10.1785/0120140247

Shirzaei, M., & Bürgmann, R. (2018). Global climate change and local land subsidence exacerbate inundation risk to the San Francisco Bay Area. *Science Advances*, *4*(3), eaap9234. https://doi.org/10.1126/sciadv.aap9234

Tape, C., Musé, P., Simons, M., Dong, D., & Webb, F. (2009). Multiscale estimation of GPS velocity fields. *Geophysical Journal International*, *179*(2), 945–971. https://doi.org/10.1111/j.1365-246X.2009.04337.x

Tong, X., Sandwell, D. T., & Smith-Konter, B. (2013). High-resolution interseismic velocity data along the San Andreas Fault from GPS and InSAR. *Journal of Geophysical Research: Solid Earth*, *118*(1), 369–389. https://doi.org/10.1029/2012jb009442

Tymofyeyeva, E., & Fialko, Y. A. (2017). *3-component time-dependent crustal deformation in Southern California from Sentnel-1 and GPS*. AGU Fall Meeting (abstract).

Wang, H., & Wright, T. J. (2012). Satellite geodetic imaging reveals internal deformation of western Tibet. *Geophysical Research Letters*, *39*, L07303. https://doi.org/10.1029/2012GL051222

Wang, K., Zhu, Y., Nissen, E., & Shen, Z. K. (2021). On the relevance of geodetic deformation rates to earthquake potential. *Geophysical Research Letters*, *48*(11), e2021GL093231. https://doi.org/10.1029/2021GL093231

Ward, L. A., Smith-Konter, B. R., Xu, X., & Sandwell, D. T. (2021). Seismic moment accumulation response to lateral crustal variations of the San Andreas Fault System. *Journal of Geophysical Research: Solid Earth*, *126*(4), e2020JB021208. https://doi.org/10.1029/2020jb021208

Ward, S. N. (1994). A multidisciplinary approach to seismic hazard in southern California. *Bulletin of the Seismological Society of America*, *84*(5), 1293–1309. https://doi.org/10.1785/bssa0840051293

Wei, S., Fielding, E., Leprince, S., Sladen, A., Avouac, J. P., Helmberger, D., et al. (2011). Superficial simplicity of the 2010 El Mayor–Cucapah earthquake of Baja California in Mexico. *Nature Geoscience*, *4*(9), 615–618. https://doi.org/10.1038/ngeo1213

Weiss, J. R., Walters, R. J., Morishita, Y., Wright, T. J., Lazecky, M., Wang, H., et al. (2020). High-resolution surface velocities and strain for Anatolia from Sentinel-1 InSAR and GNSS data. *Geophysical Research Letters*, *47*(17), e2020GL087376. https://doi.org/10.1029/2020gl087376

Weldon, R. J., Schmidt, D. A., Austin, L. J., Weldon, E. M., & Dawson, T. E. (2013). *Appendix D: Compilation of creep rate data for California faults and calculation of moment reduction due to creep*. Open-file report 2013-1165-D. US Geolgical Survey.

Wesnousky, S. G. (1986). Earthquakes, Quaternary faults, and seismic hazard in California. *Journal of Geophysical Research*, *91*(B12), 12587–12631. https://doi.org/10.1029/jb091ib12p12587

Wesnousky, S. G., Bormann, J. M., Kreemer, C., Hammond, W. C., & Brune, J. N. (2012). Neotectonics, geodesy, and seismic hazard in the northern Walker Lane of western North America; thirty kilometers of crustal shear and no strike-slip? *Earth and Planetary Science Letters*, *329–330*, 133–140. https://doi.org/10.1016/j.epsl.2012.02.018

Wessel, P., Luis, J. F., Uieda, L., Scharroo, R., Wobbe, F., Smith, W. H. F., & Tian, D. (2019). The generic mapping tools version 6. *Geochemistry, Geophysics, Geosystems*, *20*(11), 5556–5564. https://doi.org/10.1029/2019GC008515

Working Group on California Earthquake Probabilities. (1995). Seismic hazards in southern California: Probable earthquakes, 1994 to 2024. *Bulletin of the Seismological Society of America*, *85*(2), 379–439.

Wright, T., Houseman, G., Fang, J., Maghsoudi, Y., Hooper, A., Elliott, J., et al. (2023). High-resolution geodetic strain rate field reveals internal deformation of Tibetan Plateau. *EarthArXiv*. [Preprint]. https://doi.org/10.31223/X5G95R

Xu, X., Sandwell, D. T., Klein, E., & Bock, Y. (2021). Integrated Sentinel-1 InSAR and GNSS time-series along the San Andreas fault system. *Journal of Geophysical Research: Solid Earth*, *126*(11), e2021JB022579. https://doi.org/10.1029/2021JB022579

Xu, X., Sandwell, D. T., Tymofyeyeva, E., Gonzalez-Ortega, A., & Tong, X. (2017). Tectonic and anthropogenic deformation at the Cerro Prieto geothermal step-over revealed by Sentinel-1A InSAR. *IEEE Transactions on Geoscience and Remote Sensing*, *55*(9), 5284–5292. https://doi.org/10.1109/tgrs.2017.2704593

Yan, H., Dai, W., Liu, H., Gao, H., Neely, W. R., & Xu, W. (2022). Fusion of spatially heterogeneous GNSS and InSAR deformation data using a multiresolution segmentation algorithm and its application in the inversion of slip distribution. *Remote Sensing*, *14*(14), 3293. https://doi.org/10.3390/rs14143293

Zeng, Y. (2022a). GPS velocity field of the western United States for the 2023 National Seismic Hazard Model Update. *Seismological Society of America*, *93*(6), 3121–3134. https://doi.org/10.1785/0220220180

Zeng, Y. (2022b). A fault-based crustal deformation model with deep driven dislocation sources for the 2023 update to the US National Seismic Hazard Model. *Seismological Society of America*, *93*(6), 3170–3185. https://doi.org/10.1785/0220220209

Zheng, Y. J., Fattahi, H., Agram, P., Simons, M., & Rosen, P. (2022). On closure phase and systematic bias in multilooked SAR interferometry. *IEEE Transactions on Geoscience and Remote Sensing*, *60*, 1–11. https://doi.org/10.1109/TGRS.2022.3167648

Zuza, A. V., & Cao, W. (2020). Seismogenic thickness of California: Implications for thermal structure and seismic hazard. *Tectonophysics*, *782*, 228426. https://doi.org/10.1016/j.tecto.2020.228426